Implementation of an Aeroelasticity Tool for Compressor Blade and Vane Vibratory Stress Prediction using ANSYS and CFX

Nicola Houle

A thesis submitted to McGill University in
partial fulfillment of the requirements of the degree of
Master's of science
Department of Mechanical Engineering

Acronyms

APU Auxiliary Power Unit 1

BC Boundary Condition 8, 23, 24, 29–35, 45, 46, 51

CFD Computational Fluid Dynamics ix, xi, 1, 2, 4, 5, 7, 11, 20–24, 32–35, 38–41, 47–52

DNS Direct Numerical Simulation 4
DOF Degrees Of Freedom 14, 18, 19, 30, 34, 35, 44–46

EO Engine Order 27, 36, 43

FE Finite Element ix, 1, 2, 11, 12, 20–26, 29, 30, 36, 38–40, 44–46, 48, 51
FFT Fast Fourier Transform 23, 36
FSI Fluid-Structure Interaction 2
FV Finite Volume 11

HCF High Cycle Fatigue 1

IBR Integrated Bladed Rotor 25, 29
IC Initial Condition 38

LES Large Eddy Simulation 50, 52
LSB Laminar Separation Bubble 49

ND Nodal Diameter 29, 31, 32, 44, 46, 47
NS Navier-Stokes 3, 4
NSMS Non-Intrusive Stress Measurement System ix, 1

P&WC Pratt & Whitney Canada v, vii, ix, xi, 1, 2, 21, 51
PT Power Turbine 24

RANS Reynolds Averaged Navier-Stokes 4, 5, 7, 9, 11, 22, 24, 34, 36, 50, 51

SDOF Single Degree Of Freedom 36, 37, 48, 49

TBR Transient Blade Row 7, 10, 22, 24, 36, 39, 48

Dedication

This thesis is dedicated to my manager at Pratt & Whitney Canada (P&WC), Mr. Aldo Abate. Mr. Abate has been working extremely hard in the last five to ten years to initiate an aeroelasticity research project for building a vibratory stress prediction tool. This work would have simply never been realized without Mr. Abate's desire for it and without his hard work for finding ways to fund it.

Finally, this thesis and this work is dedicated to the ones who will never read my thesis nor hear about me, my thesis advisor, or my colleagues at P&WC. It is dedicated to the thousands of people who use airplanes and helicopters every day as a means of transportation. Dear public, you are the reason why engineers keep innovating and improving their techniques and their science. This project will help to improve engine compressor blade and vane designs for reducing chances of failure during operation. This will therefore help to design safer engines for you and I am grateful and proud to be at your service.

Acknowledgments

I would first like to thank my thesis advisor, Prof. Mathias Legrand of the Mechanical Engineering Department at McGill University and my manager at P&WC, Mr. Aldo Abate, Component Dynamics manager and fellow of dynamics. The doors of Prof. Legrand and Mr. Abate were always open whenever I ran into any type of issues or whenever I had any questions regarding my research or writing. Prof. Legrand's rigour in his attention to details regarding engineering science, technical presentations, and thesis redaction tremendously improved my skills in these areas. On the other hand, Mr. Abate never hesitated to put his technical expertise and his very sharp sixth sense in dynamics at my disposal for transmitting his knowledge to me. Because of him, I have learned a lot about challenges in dynamics and how to solve them.

A very special thank you to Mr. Feng Shi, Compressor Aerodynamics engineer at P&WC and his manager, Mr. Peter Townsend, Compressor Aerodynamics manager. I must admit that I would never have been able to understand CFX modelling well enough for doing this project without Mr. Shi's fantastic support and I thank him very much for his great help. Thank you Mr. Townsend for all your very useful advises in aerodynamics which were a great support for this project.

A very important thank you to Mr. Denis Lavoie, retired Component Dynamics principal engineer. Mr. Lavoie was a great mentor for me and introduced me to the world of dynamics, taught me all the fundamentals, and, most important, transmitted his passion about dynamics to me which is essential.

Thank you to all my other colleagues in Component Dynamics, especially Dr. Krishna Balike, Component Dynamics engineer and Dr. Ignatius Theratil, Component Dynamics principal engineer who gave me very good insight to help me with my project. Their help was essential and really made the difference.

Thank you as well to Mr. Barry Barnett, Product Technology Development principal project engineer and Mr. Eric Ho, Structural Systems principal engineer for helping in funding this project and offering their opinions and point of views as the project was progressing.

Finally, I must express my very profound gratitude to my parents Chantal and Serge, my fiancée Jennifer, and the other members of my fantastic family for providing me with unfailing and unconditional support and encouragement throughout my years of study and throughout the process of research and writing this thesis. The accomplishment would not have been possible without them. Thank you.

Abstract

Modal analyses with engine tests are the common tools used by P&WC to measure vibratory stress levels on compressor blades and vanes subjected to aerodynamic excitation. Vibratory stress levels are accurately measured with strain gauges and Non-Intrusive Stress Measurement System (NSMS) probes during engine tests. A numerical tool predicting vibratory stress levels on these components would help to do a more mature assessment of their designs and redesigns. Such a tool would shave off redesign iterations, time, and possibly engine test iterations.

Two good test case candidates, one blade and one vane, were chosen by P&WC for building the aeroelasticity tool. The steady and unsteady Computational Fluid Dynamics (CFD) analyses were performed using CFX and the Finite Element (FE) analyses were performed with ANSYS. Vibratory stress levels were calculated using harmonic response and transient one-way aeroelasticity analyses. A two-way aeroelasticity analysis was also attempted.

For the investigated resonance on the blade test case, the calculated vibratory stress levels were 1.34% higher than the stress levels measured during strain gauge test. For the vane, the engine was tested with two different inlet temperatures. The second inlet temperature was 50% higher than the first one. This increased the maximum vibratory stress levels by 35.9%. The calculated vibratory stress levels were 29.2% less than in test for the first inlet temperature and 41.1% less than in test with the second one. The presence of separated flow regions is a potential source of error.

Two-way aeroelasticity was also attempted on the blade test case, but failed due to mesh folding in the CFD domain. This issue shall be resolved during future work.

Abrégé

Les analyses modales utilisées conjointement avec des données de tests moteur sont les outils exploités par P&WC pour la mesure de contraintes vibratoires sur les ailettes et les redresseurs assujettis à des excitations aérodynamiques dans un compresseur. Ces tests moteur sont effectués avec des jauges de contraintes et des capteurs non intrusifs pour la mesure de contraintes. Un outil numérique calculant les contraintes vibratoires sur ces composantes permettrait une évaluation plus mature de leurs conceptions et modifications de conceptions. Un tel outil épargnerait des itérations de modification de conceptions, du temps et possiblement des tests.

Deux bons candidats, une ailette et un redresseur, furent choisis par P&WC pour créer cet outil d'analyse aéroélastique. Les analyses numériques en dynamique des fluides (ou CFD) statiques et transitoires furent déployées avec le logiciel CFX et les analyses d'éléments finis avec le logiciel ANSYS. Les contraintes vibratoires furent calculées avec les méthodes d'analyse aéroélastiques unidirectionnelles par réponse harmonique et transitoire. Une analyse aéroélastique bidirectionnelle fut également déployée.

Concernant la résonance de l'ailette, les contraintes vibratoires calculées sont 1,34% supérieures à celles mesurées en test. Pour le redresseur, le moteur fut testé avec deux températures d'admissions différentes. La seconde température était 50% supérieure à la première. Cette montée en température d'admission a augmenté les contraintes vibratoires maximales de 35,9%. Les contraintes vibratoires calculées furent 29,2% inférieures à celles mesurées en test pour la première température et 41,1% inférieures à celles mesurées en test pour la seconde température. La présence de régions d'écoulements fractionnés pourrait être la cause de ces erreurs.

L'analyse d'aéroélasticité bidirectionnelle a été déployée sur l'ailette, cependant cette analyse a échoué à cause d'un problème de repliement de maillage dans le domaine du fluide. Ce problème devra être résolu à l'avenir.

Contents

Chapter 1

Introduction

1.1 Problem Statement

The goal of this work was to implement a numerical aeroelasticity tool for vibratory stress levels prediction at P&WC. This was an industrial project partially financed by MITACS Accelerate. This numerical aeroelasticity tool uses CFD and FE techniques that are well known in the academic world. The project was therefore focused on the implementation and validation of the numerical aeroelasticity tool in an industry and not on academic research.

Present in the turboshaft, turbopropeller, turbofan, and Auxiliary Power Unit (APU) businesses, P&WC, a United Technologies company, has more than 52,000 engines in service powering the largest fleet of business and regional aircraft and helicopters over 200 countries and territories. Every second, a P&WC powered aircraft takes off or lands somewhere in the world. To preserve its leadership in the aeronautical industry, P&WC engineers must use the latest technologies and methodologies in their product design and redesign phases.

Avoiding High Cycle Fatigue (HCF) in compressor blades and vanes is one of the numerous design and redesign challenges faced by P&WC engineers everyday. To know whether a compressor blade or vane design or redesign will undergo HCF issues, the vibratory stress distribution in the geometry must be known for every mode resonating during engine operation. The best way to find the vibratory stress levels on compressor blades or vanes is to instrument these components with strain gauges or NSMS probes, assemble them on an engine, and run it in a test cell. The data collected by the instrumentation and FE modal analyses results give an accurate assessment of the induced vibratory stress levels on compressor blades or vanes during engine operation. With this assessment in hand, it can be found out whether the parts will have HCF issues or not. If necessary, the assessment will also provide guidance for launching a redesign action for making the components satisfactory in terms of HCF.

This methodology is the one currently used by the Component Dynamics engineers at P&WC. Unfortunately, running an instrumented engine test costs hundreds of thousands of dollars; therefore, if several redesign iterations are required for converging towards a satisfactory design, the overall design cost may be quite high due to the time spent on the redesign activities and especially the engine test iterations. Accordingly, it would be beneficial for P&WC to have a numerical tool for calculating the vibratory stress levels of the modes in resonance during engine operation. Such a vibratory stress prediction tool would help P&WC to perform more mature assessments of their compressor blades and vanes designs and redesigns. Also, it would potentially help the engineers to converge faster towards a satisfactory design shaving off time, engine tests iterations, and design costs.

For a numerical tool to calculate accurate vibratory stress values on a compressor blade or vane, it has to compute accurately the excitation and the dynamic response of the geometry subjected to this excitation. For compressor blades and vanes, the excitation is aerodynamic.

When rotating, a compressor blade undergoes periodic excitation in space and time from the wakes of the upstream vane rows and from the bow waves of the downstream vane rows. On the other hand, a compressor vane undergoes periodic excitation in space and time from the wakes of the upstream rotating blades and from the bow waves of the downstream rotating blades. Therefore, an adequate vibratory stress prediction tool for compressor blades and vanes must be performing transient CFD and FE analyses. These CFD and FE interactions are called aeroelasticity or Fluid-Structure Interaction (FSI) analyses.

At P&WC, Compressor Aerodynamics engineers use the CFX software, an ANSYS product, for CFD analyses and Component Dynamics engineers use the ANSYS software for FE analyses. Therefore, P&WC already has in house commercial tools capable of undertaking aeroelasticity analyses if used properly. Moreover, P&WC has accumulated a considerable amount of engine strain gauge test data of compressor blades and vanes. Therefore, P&WC has all the elements for establishing an aeroelasticity analysis procedure or tool for compressor blades and vanes. One or more compressor components could be selected for establishing the numerical analysis procedure, calculating the vibratory stress levels, and comparing them with the vibratory stress levels measured during the strain gauge tests of these components for validating the procedure.

P&WC selected a compressor rotor blade design as a candidate for developing the aeroelasticity analysis procedure. The available strain gauge data of this blade has been reviewed and the highest vibratory stress obtained during the test has been identified. One-way and two-way aeroelasticity analyses have been performed for calculating the vibratory stress levels and comparing them with the ones obtained during strain gauge test. Once the analyses were completed on the rotor blade, the established one-way aeroelasticity procedure was repeated on a stator vane.

Note that the vibratory stress levels that were investigated on the two geometries were the synchronous responses of modes in resonance. Consequently, it was known prior to the investigation that one-way and two-way aeroelasticity results should be similar. One-way aeroelasticity should have been sufficient to get good vibratory stress levels predictions. However, it has been decided to perform at least one two-way aeroelasticity attempt since this type of analysis has the capability to predict asynchronous responses like flutter. Therefore, having a two-way aeroelasticity procedure in place is beneficial if an asynchronous response prediction was needed for a compressor component.

This thesis summarizes the one-way and two-way aeroelasticity analyses conducted on the compressor blade and vane. The results with the potential sources of error are presented and the planned future work is described.

1.2 Aeroelasticity Theory

Dynamic aeroelasticity specifically is a combination of three disciplines: dynamics, fluid mechanics, and solid mechanics. These three disciplines are widely used in the mechanical engineering field. In mechanical engineering, fluid mechanics is used for the study of aerodynamics, solid mechanics is used for the study of elastic forces in solids, and dynamics is used for the study of inertial forces and motion [5].

As shown in figure 1.1, there are two types of aeroelasticity: static aeroelasticity and dynamic aeroelasticity. Static aeroelasticity regroups the aerodynamic forces and the elastic forces. Since the inertial forces are not present, this type of aeroelasticity targets the static elastic forces induced on solids due to static aerodynamic forces. On the other hand, dynamic aeroelasticity regroups all three disciplines and can be used to calculate the dynamic elastic forces in a solid due to dynamic aerodynamic forces. Since the vibratory stress levels needed to be calculated on a rotating blade and a vane for this work, dynamic aeroelasticity was used.

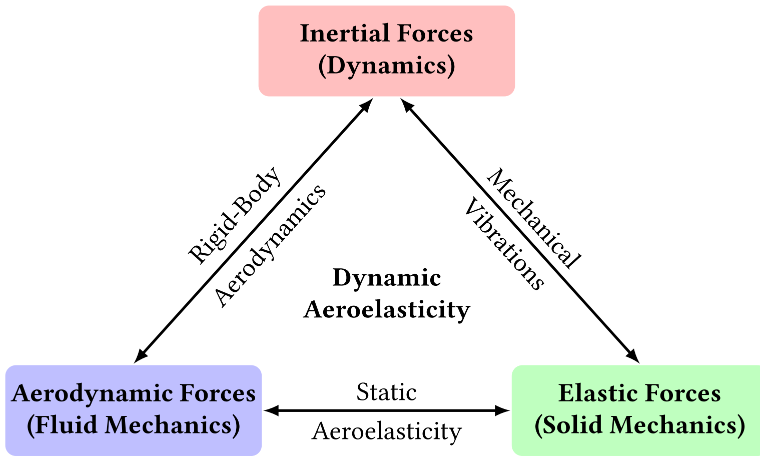

Figure 1.1: Aeroelasticity triangle

1.2.1 Dynamic Fluid Mechanics Theory

The governing equations in dynamic fluid mechanics are the continuity, momentum, and energy Navier-Stokes (NS) equations in their conservative forms [1, 6]. Every variable in these equations is space and time dependent. The continuity equation reads[1]:

$$\frac{\partial \rho}{\partial t} + \boldsymbol{\nabla} \cdot (\rho \mathbf{u}) = 0, \quad \forall m \in \Omega_{\mathrm{f}}, \quad \forall t > 0 \tag{1.1}$$

where ρ is the density, $\mathbf{u}$, the velocity vector, m, any point in the three dimensional space, Ω_{f}, the applicable fluid domain, and t, the time. The momentum equation reads:

$$\frac{\partial (\rho \mathbf{u})}{\partial t} + \boldsymbol{\nabla} \cdot (\rho \mathbf{u} \times \mathbf{u}) = -\boldsymbol{\nabla} p + \boldsymbol{\nabla} \cdot \boldsymbol{\tau} + \rho \mathbf{f}_{\mathrm{ext}} \tag{1.2}$$

where p is the static pressure, $\mathbf{f}_{\mathrm{ext}}$ the external force vector per unit mass, and $\boldsymbol{\tau}$ the shear stress tensor.

For a Newtonian fluid, like air, the shear stress tensor relation to the strain rate reads:

$$\boldsymbol{\tau} = \mu \left(\boldsymbol{\nabla} \mathbf{u} + \boldsymbol{\nabla}^T \mathbf{u} - \frac{2}{3} \delta \boldsymbol{\nabla} \cdot \mathbf{u} \right) \tag{1.3}$$

where μ is the dynamic (or shear) viscosity and δ the Kronecker delta function. The momentum equation specific to Newtonian fluids can then be constructed by substituting equation (1.3) into equation (1.2), which reads:

$$\frac{\partial (\rho \mathbf{u})}{\partial t} + \boldsymbol{\nabla} \cdot (\rho \mathbf{u} \times \mathbf{u}) = -\boldsymbol{\nabla} p + \boldsymbol{\nabla} \cdot \left(\mu \left(\boldsymbol{\nabla} \mathbf{u} + \boldsymbol{\nabla}^T \mathbf{u} - \frac{2}{3} \delta \boldsymbol{\nabla} \cdot \mathbf{u} \right) \right) + \rho \mathbf{f}_{\mathrm{ext}} \tag{1.4}$$

[1] Equations (1.1) to (1.12) are true $\forall m \in \Omega_{\mathrm{f}}$ and $\forall t > 0$. Consequently, it will not be specified systematically at every equation.

The total energy equation reads:

$$\frac{\partial(\rho h_{\mathrm{tot}})}{\partial t} - \frac{\partial p}{\partial t} + \boldsymbol{\nabla} \cdot (\rho \mathbf{u} h_{\mathrm{tot}}) = \boldsymbol{\nabla} \cdot (\lambda \boldsymbol{\nabla} T) + \boldsymbol{\nabla} \cdot (\mathbf{u} \cdot \boldsymbol{\tau}) + \mathbf{u} \cdot \rho \mathbf{f}_{\mathrm{ext}} + E_{\mathrm{ext}} \tag{1.5}$$

where h_{tot} is the total enthalpy, λ the thermal conductivity, T the temperature, and E_{ext} the external energy. The total enthalpy is the sum of the static enthalpy and the kinetic energy which is:

$$h_{\mathrm{tot}} = h + \frac{1}{2} \parallel \mathbf{u} \parallel^2 \tag{1.6}$$

Reynolds Averaged Navier-Stokes Equations

The CFD analyses conducted in this work were steady and unsteady three dimensional analyses of transonic PT6 engine compressors. Accordingly, some regions in the fluid domains had very high Reynolds numbers. This means that the fluid models were turbulent. The assumptions for incompressible or inviscid flow were both obviously not valid. Therefore, the NS equations demonstrated previously were the appropriate ones for CFD problems of this type since they describe both laminar and turbulent flows.

However, turbulent flows involved in realistic problems include large turbulent regions compared to the overall size of the domain and large time scales compared to the total time. Therefore, to perform a Direct Numerical Simulation (DNS) of the NS equations accurately, a mesh much smaller than the smallest suitable meshes used in numerical analyses is required. So, performing DNS of these equations would require tremendously more computational power than available today.

To account for the effects of turbulence while using a convenient mesh size for numerical analyses, it can be assumed that the turbulent regions in the flow exhibit average and fluctuating characteristics. This assumption is introduced in the NS equations by imposing the velocity ($\mathbf{u}$) to be composed of an average term and a fluctuating term. Imposing this assumption on the NS equations leads to the Reynolds Averaged Navier-Stokes (RANS) equations. The RANS equations solve for the mean flow quantities only. They do model the turbulence effects, but without the need for the resolution of the fluctuations. Hence, the required mesh refinement and computational power are much less than if DNS of the NS equations was performed [8].

Since the RANS equations are composed of the same variables as the NS equations, every variable in these equations is space and time dependent. As stated above, RANS equations are constructed by imposing the velocity to be composed of an average term and a fluctuating term:

$$\mathbf{u} = \overline{\mathbf{u}} + \mathbf{u}_{\mathrm{f}} \tag{1.7}$$

where the average term reads:

$$\overline{\mathbf{u}} = \frac{1}{\Delta t} \int_t^{t+\Delta t} \mathbf{u} dt \tag{1.8}$$

and where Δt is a large time scale with respect to the turbulent fluctuations, but small with respect to the total time of the analysis in question.

Substituting the averaged quantities into the NS equations gives the RANS equations. The averaged continuity equation reads:

$$\frac{\partial \rho}{\partial t} + \boldsymbol{\nabla} \cdot (\rho \overline{\mathbf{u}}) = 0 \tag{1.9}$$

It can be observed that the continuity equation is not altered, but the averaged form of the momentum and energy equations contain some additional turbulent flux terms. The averaged momentum equation reads:

$$\frac{\partial(\rho\overline{\mathbf{u}})}{\partial t} + \boldsymbol{\nabla}\cdot(\rho\overline{\mathbf{u}}\times\overline{\mathbf{u}}) = -\boldsymbol{\nabla}p + \boldsymbol{\nabla}\cdot(\boldsymbol{\tau} - \rho\overline{\mathbf{u}}_{\mathrm{f}}\times\overline{\mathbf{u}}_{\mathrm{f}}) + \rho\mathbf{f}_{\mathrm{ext}} \tag{1.10}$$

and the averaged total energy equation reads:

$$\frac{\partial(\rho h_{\mathrm{tot}})}{\partial t} - \frac{\partial p}{\partial t} + \boldsymbol{\nabla}\cdot(\rho\overline{\mathbf{u}}h_{\mathrm{tot}}) = \boldsymbol{\nabla}\cdot(\lambda\boldsymbol{\nabla}T - \rho\overline{\mathbf{u}_{\mathrm{f}}h}) + \boldsymbol{\nabla}\cdot(\mathbf{u}\cdot(\boldsymbol{\tau} - \rho\overline{\mathbf{u}}_{\mathrm{f}}\times\overline{\mathbf{u}}_{\mathrm{f}})) + \mathbf{u}\cdot\rho\mathbf{f}_{\mathrm{ext}} + E_{\mathrm{ext}} \tag{1.11}$$

It is also important to note that the total enthalpy (h_{tot}) contains a turbulent kinetic energy term which was not present in equation (1.6). The total enthalpy including the turbulent kinetic energy term reads:

$$h_{\mathrm{tot}} = h + \frac{1}{2}\left(\parallel \overline{\mathbf{u}} \parallel^2 + \parallel \overline{\mathbf{u}}_{\mathrm{f}} \parallel^2 \right) \tag{1.12}$$

Equations (1.9) through (1.12) form the RANS equations. They are the ones which are discretised and programmed in the CFX solver used for solving the CFD analyses in this work.

The Mixing Plane Concept in Steady CFD Analyses

In the steady CFD analyses of this project, the time independent RANS equations were solved. These equations are the RANS equations, but without the time derivative terms. The time independent RANS equations are still nonlinear and must be solved by iteration until the residual convergence criteria are met.

When doing steady CFD analyses in turbomachines composed of blade and vane rows, the conventional method is to model only one passage of every blade and vane row and apply the usual cyclic conditions at the boundaries where every passage mates with the adjacent ones. Conventional cyclic modelling method is shown in figure 1.2 where cyclic conditions are applied on the $\partial\Omega_{\mathrm{R}_1}$, $\partial\Omega_{\mathrm{R}_2}$, $\partial\Omega_{\mathrm{S}_1}$, and $\partial\Omega_{\mathrm{S}_2}$ boundaries.

However, the number of blades and vanes is often not the same in turbomachine rows. So, conventional cyclic method is inadequate since modelling one passage per row results in non-unity pitch ratios. This is the case of the rotor and stator passages shown in figure 1.2 since $P_{\mathrm{R}} \neq P_{\mathrm{S}}$ which is a typical scenario in a real compressor. The mixing plane concept is therefore used for computing steady CFD analyses by using cyclic conditions on a model composed of one passage per row.

The idea behind this concept is that every passage is considered as a single domain which can be meshed independently. The plane where the rotor and stator domains mate is called the mixing plane and it is shown in figure 1.2. While converging the residual of the the time independent RANS equations, the following averaged quantity transfers are performed at the mixing plane

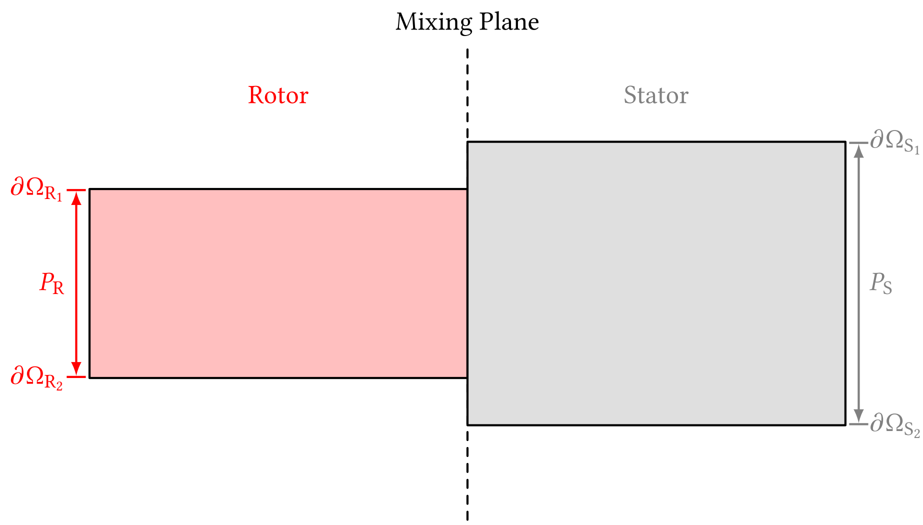

Figure 1.2: Cyclic analysis with non-unity pitch ratio

after every residual convergence iteration:

$$\begin{aligned}
\overline{p}_0, \quad &\forall m \in \partial\Omega_\mathrm{u} \rightarrow \overline{p}_0, \quad \forall m \in \partial\Omega_\mathrm{d} \\
\overline{\hat{\mathbf{t}}}_\mathrm{f}, \quad &\forall m \in \partial\Omega_\mathrm{u} \rightarrow \overline{\hat{\mathbf{t}}}_\mathrm{f}, \quad \forall m \in \partial\Omega_\mathrm{d} \\
\overline{T}_0, \quad &\forall m \in \partial\Omega_\mathrm{u} \rightarrow \overline{T}_0, \quad \forall m \in \partial\Omega_\mathrm{d} \\
\overline{k}_\mathrm{t}, \quad &\forall m \in \partial\Omega_\mathrm{u} \rightarrow \overline{k}_\mathrm{t}, \quad \forall m \in \partial\Omega_\mathrm{d} \\
\overline{\epsilon}_\mathrm{t}, \quad &\forall m \in \partial\Omega_\mathrm{u} \rightarrow \overline{\epsilon}_\mathrm{t}, \quad \forall m \in \partial\Omega_\mathrm{d} \\
\overline{p}_\mathrm{s}, \quad &\forall m \in \partial\Omega_\mathrm{d} \rightarrow \overline{p}_\mathrm{s}, \quad \forall m \in \partial\Omega_\mathrm{u} \\
\overline{\hat{\mathbf{t}}}_\mathrm{f}, \quad &\forall m \in \partial\Omega_\mathrm{d} \rightarrow \overline{\hat{\mathbf{t}}}_\mathrm{f}, \quad \forall m \in \partial\Omega_\mathrm{u}
\end{aligned} \tag{1.13}$$

where $\overline{p}_0$ is the average total pressure, $\overline{\hat{\mathbf{t}}}_\mathrm{f}$ the average flow tangential unit vector in cylindrical coordinates, $\overline{T}_0$ the average total pressure, $\overline{k}_\mathrm{t}$ the average turbulence kinetic energy, $\overline{\epsilon}_\mathrm{t}$ the average dissipation rate, $\overline{p}_\mathrm{s}$ the average static pressure, m any point belonging to the three dimensional space, $\partial\Omega_\mathrm{u}$ the boundary of the upstream domain at the mixing plane, and $\partial\Omega_\mathrm{d}$ the boundary of the downstream domain at the mixing plane.

Since averaged values are considered at the mixing plane, it is highly recommended to use this method only when the flow is uniform at the mixing plane. Otherwise, results obtained with this method are not meaningful. Furthermore, when using this approach, any unsteadiness that may arise in the flow (e.g. shock waves, wakes, separated flows) are not transmitted from one passage to another. Despite these consequences, the mixing plane concept provides a very good approximation of the time averaged flow [9].

There are two well known methods for averaging the flow variables at the mixing plane on $\partial\Omega_\mathrm{u}$ and $\partial\Omega_\mathrm{d}$. These methods are the area averaging and mass averaging methods. With the area averaging method, every flow variable (f_v) is averaged on $\partial\Omega_\mathrm{u}$ and $\partial\Omega_\mathrm{d}$ as follows:

$$\begin{aligned} \overline{f}_{\mathrm{v_u}} &= \frac{1}{s_\mathrm{u}} \int_{\partial\Omega_\mathrm{u}} f_{\mathrm{v_u}} ds_\mathrm{u} \\ \overline{f}_{\mathrm{v_d}} &= \frac{1}{s_\mathrm{d}} \int_{\partial\Omega_\mathrm{d}} f_{\mathrm{v_d}} ds_\mathrm{d} \end{aligned} \tag{1.14}$$

where s_u and s_d are the surface areas of $\partial\Omega_\mathrm{u}$ and $\partial\Omega_\mathrm{d}$ respectively and where $f_{\mathrm{v_u}}$ and $f_{\mathrm{v_d}}$ are the flow variables on $\partial\Omega_\mathrm{u}$ and $\partial\Omega_\mathrm{d}$ respectively. The area averaging method is the one that was used in this work for solving the steady CFD analyses.

Transient Blade Row Modelling in Unsteady CFD Analyses

Since dynamic aeroelasticity was undertaken, transient CFD analyses of the compressor blade and vane rows were performed. When performing transient CFD analyses, the full set of RANS equations is solved. In this work, time domain solving was performed using the second order backward Euler method scheme.

Again, the best approach in terms of computational effort and time is to model only one passage of every blade and vane row. However, the mixing plane concept described earlier is not appropriate for transient analyses because any unsteadiness in the flow (e.g. shock waves, wakes, separated flows) is not transmitted from one passage to another.

The classical workaround for such an unsteady CFD analysis with a non-unity pitch ratio is to deploy the pitch scaling method which is also known as profile transformation method. As shown in figure 1.3, this method consists in duplicating the blade and vane passages to bring the pitch ratio to unity ($P_\mathrm{R} = P_\mathrm{S}$). If one of the components has a prime number of blades or vanes, (e.g. if the rotor or the stator has 37 blades or vanes), a unity pitch ratio cannot be obtained unless all the passages of the rotor and the stator are modelled (full 360° analysis). This is very costly in terms of computational resources and time. In CFX, an alternative to the profile transformation approach is to use the Transient Blade Row (TBR) approach. The TBR approach handles non-unity pitch ratios through either a time transformation method or a Fourier transformation method. This method cannot be used if the fluid domain undergoes mesh deformation which is the case in a two-way aeroelasticity analysis [8].

The time and Fourier transformation methods both achieve phase-shifted cyclic conditions. When phase-shifted cyclic conditions are achieved, the pitch-wise boundaries ($\partial\Omega_{\mathrm{R_1}}/\partial\Omega_{\mathrm{R_2}}$ and $\partial\Omega_{\mathrm{S_1}}/\partial\Omega_{\mathrm{S_2}}$) are periodic to each other at different times as shown in figure 1.4 where the rotor-stator relative position (P_rel) is the same at times $t = t_0 - \Delta t$ and $t = t_0$. The time step size (Δt) reads:

$$\Delta t = \frac{P_\mathrm{S} - P_\mathrm{R}}{\Omega_\mathrm{R}} \tag{1.15}$$

where Ω_R is the rotational velocity of the rotor. In this work, transient CFD analyses were performed using the TBR approach with the time transformation method. Therefore, only this method is described in detail in this section.

The time transformation method handles the unequal pitch problem by transforming the time coordinates in the circumferential direction to make the model fully cyclic in the transformed

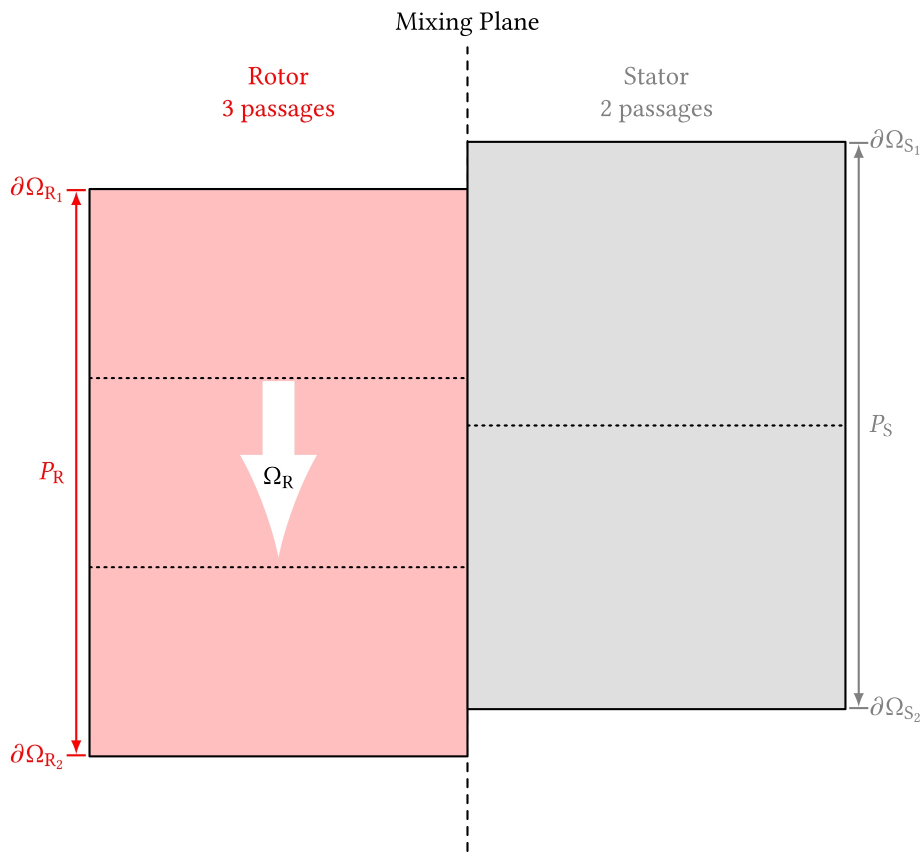

Figure 1.3: Cyclic analysis with pitch scaling approach

time domain. In cylindrical coordinates, every flow variable (f_v) is space and time dependent:

$$f_v = f_v(r, \theta, z, t), \quad \forall r, \theta, z \in \Omega_{RS}, \quad \forall t > 0 \tag{1.16}$$

where Ω_{RS} is the domain of the rotor and the stator which is a volume. Consequently, the flow variables on the four cyclic faces ($\partial\Omega_{R_1}$, $\partial\Omega_{R_2}$, $\partial\Omega_{S_1}$, and $\partial\Omega_{S_2}$) can be defined as:

$$\begin{aligned}
f_{vR_1} &= f_{vR_1}(r_{R_1}, \theta_{R_1}, z_{R_1}, t), \quad \forall r_{R_1}, \theta_{R_1}, z_{R_1} \in \partial\Omega_{R_1}, \quad \forall t > 0 \\
f_{vR_2} &= f_{vR_2}(r_{R_2}, \theta_{R_2}, z_{R_2}, t), \quad \forall r_{R_2}, \theta_{R_2}, z_{R_2} \in \partial\Omega_{R_2}, \quad \forall t > 0 \\
f_{vS_1} &= f_{vS_1}(r_{S_1}, \theta_{S_1}, z_{S_1}, t), \quad \forall r_{S_1}, \theta_{S_1}, z_{S_1} \in \partial\Omega_{S_1}, \quad \forall t > 0 \\
f_{vS_2} &= f_{vS_2}(r_{S_2}, \theta_{S_2}, z_{S_2}, t), \quad \forall r_{S_2}, \theta_{S_2}, z_{S_2} \in \partial\Omega_{S_2}, \quad \forall t > 0
\end{aligned} \tag{1.17}$$

The flow variables spatial cyclic boundary conditions on both passages read:

$$\begin{aligned}
f_{vR_1}(r_{R_1}, \theta_{R_1}, z_{R_1}, t) &= f_{vR_2}(r_{R_2}, \theta_{R_2} + P_R, z_{R_2}, t - \Delta t) \\
f_{vS_1}(r_{S_1}, \theta_{S_1}, z_{S_1}, t) &= f_{vS_2}(r_{S_2}, \theta_{S_2} + P_S, z_{S_2}, t - \Delta t)
\end{aligned} \tag{1.18}$$

where Δt is as per equation (1.15). The appropriate time transformation for making the model

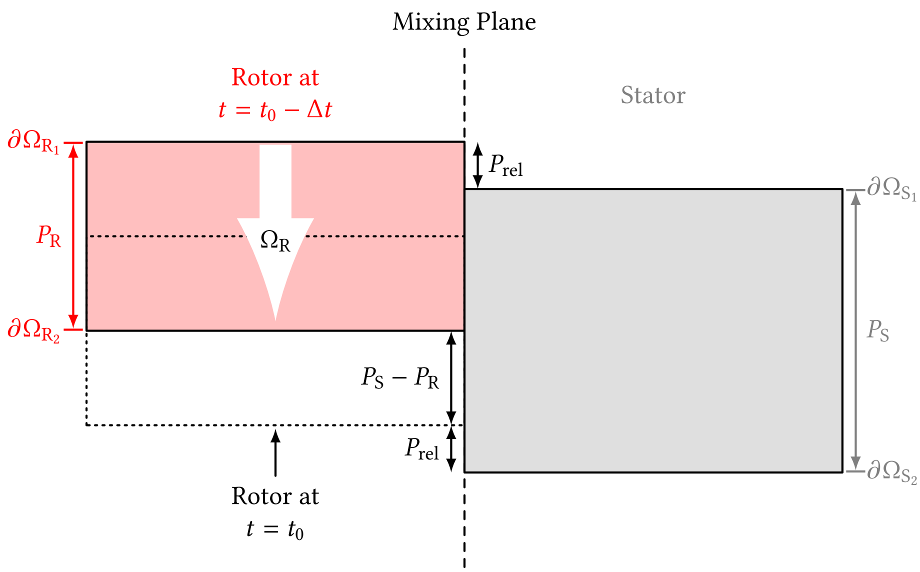

Figure 1.4: Cyclic analysis with time shifted boundary conditions

fully cyclic is:

$$\begin{aligned} r' &= r \\ \theta' &= \theta \\ z' &= z \\ t' &= t - \lambda_{R,S}\theta \end{aligned} \tag{1.19}$$

where

$$\lambda_{R,S} = \frac{\Delta t}{P_{R,S}} \tag{1.20}$$

and where $P_{R,S}$ is the pitch of the rotor from the stator frame of reference.

Imposing the set of space-time transformations in equation (1.19) to the cyclic conditions of equations (1.18) yields to regular spatial Boundary Condition (BC)s which are:

$$\begin{aligned} f_{v_{R_1}}(r'_{R_1}, \theta'_{R_1}, z'_{R_1}, t') &= f_{v_{R_2}}(r'_{R_2}, \theta'_{R_2} + P_R, z'_{R_2}, t') \\ f_{v_{S_1}}(r'_{S_1}, \theta'_{S_1}, z'_{S_1}, t') &= f_{v_{S_2}}(r'_{S_2}, \theta'_{S_2} + P_S, z'_{S_2}, t') \end{aligned} \tag{1.21}$$

With this set of cyclic conditions, a fully cyclic model is obtained and periodicity is maintained at any instant in the transformed time domain. This can be visualized in the physical time vs. circumferential direction graph in figure 1.5. It can be seen in this figure that the rotor pitch is smaller than the stator pitch in the physical time domain. However, their boundaries match in the transformed time domain.

Therefore, the full RANS equations are solved in the transformed domain described above. Since a fully cyclic model is obtained in the transformed domain, the flow variables are not averaged at the mixing plane. Accordingly, the flow unsteadiness is transmitted between the two

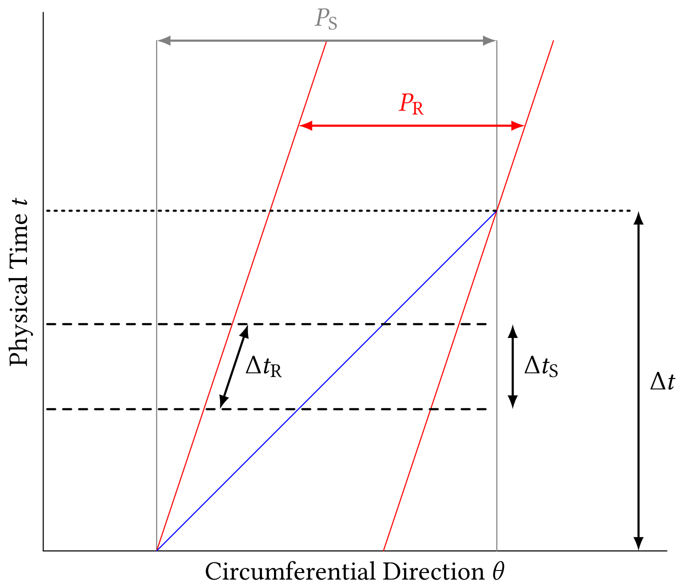

Figure 1.5: Physical boundaries: stator (—) and rotor (—); transformed time t' (—)

passages. Once the analysis is completed, meaningful results can be retrieved by switching the flow variables from transformed time domain (r', θ', z', and t') back to physical time domain (r, θ, z, and t).

As it can also be observed in figure 1.5, the rotor and the stator are marching at different time step sizes because each passage is experiencing a different period. The stator period is:

$$T_S = \frac{P_R}{\Omega_R} \tag{1.22}$$

whereas the rotor period is:

$$T_R = \frac{P_S}{\Omega_R} \tag{1.23}$$

In each passage, the period must be discretised using the same time step (h_t). So, the rotor and stator periods read:

$$T_S = h_t \Delta t_S \tag{1.24}$$

$$T_R = h_t \Delta t_R \tag{1.25}$$

where Δt_S and Δt_R are the time step sizes of the stator and the rotor respectively.

Combining equation (1.22) with equation (1.24) and equation (1.23) with equation (1.25) relates the pitch ratio to the time step sizes ratio:

$$\frac{P_R}{P_S} = \frac{\Delta t_S}{\Delta t_R} \tag{1.26}$$

When performing a transient analysis in CFX, a time step size has to be imposed. In a TBR analysis using the time transformation method, the imposed time step size is the time step size of the stator (ΔT_S). The time step size of the rotor (ΔT_R) can then be calculated using equation (1.26). Therefore, once the analysis is completed and that the variables are switched from the transformed time domain to the physical time domain, the elapsed simulation time is considered the stator simulation time. The rotor to stator time step size ratio relation with the pitch ratio demonstrated in equation (1.26) can be observed in the graph in figure 1.5.

1.2.2 Dynamic Solid Mechanics Theory

Every variable in the following dynamic linear elasticity equations are space and time dependent [4]. The local equation of linear elasticity reads[2]:

$$\rho\frac{\partial^2 \mathbf{u}}{\partial t^2} - \boldsymbol{\nabla}\cdot\boldsymbol{\sigma} = \mathbf{f}, \quad \forall m \in \Omega_s, \quad \forall t > 0 \tag{1.27}$$

where $\boldsymbol{\sigma}$ is the stress tensor, $\mathbf{f}$ the total force vector per mass unit, m any point in the three dimensional space, Ω_s the applicable solid domain, and t the time. The stress tensor is governed by the first constitutive law of elasticity which reads:

$$\boldsymbol{\sigma} = 2\mu_s\boldsymbol{\epsilon} + \lambda_s\,\mathrm{tr}(\boldsymbol{\epsilon})\boldsymbol{T} \tag{1.28}$$

where μ_s is the rigidity parameter, $\boldsymbol{\epsilon}$ the strain tensor, λ_s the Lame's first parameter, and $\boldsymbol{T}$ the temperature tensor. The strain tensor is governed by the second law of elasticity which reads:

$$\boldsymbol{\epsilon} = \frac{1}{2}(\boldsymbol{\nabla}\mathbf{u} + \boldsymbol{\nabla}^T\mathbf{u}) \tag{1.29}$$

Equations (1.27) through (1.29) are the linear dynamic solid mechanics equations required for solving the mechanical systems in this work. As opposed to the RANS equations which were discretised using Finite Volume (FV) for performing CFD analyses, the linear elasticity equations are discretised using FE. Therefore, the weak form of these equations is needed. The weak form reads: Find $\mathbf{u} \in U$ such that

$$\int_{\Omega s}\left(\mathbf{v}\cdot\rho\frac{\partial^2\mathbf{u}}{\partial t^2} + \boldsymbol{\sigma} : \left(\frac{1}{2}(\boldsymbol{\nabla}\mathbf{v} + \boldsymbol{\nabla}^T\mathbf{v})\right) - \mathbf{v}\cdot\mathbf{f}\right)dv - \int_{\partial\Omega_\sigma}\mathbf{t}_p\cdot\mathbf{v}ds = 0, \quad \forall\mathbf{v}\in U_0 \tag{1.30}$$

where $\partial\Omega_\sigma$ is the boundary of the domain which is a surface, $\mathbf{v}$ the test function, $\mathbf{t}_p$ is the traction force which is acting on the boundary, U the space of kinematically acceptable displacements, and U_0 the space of kinematically homogeneous displacements. Equation (1.30) combined with equations (1.28) and (1.29) are the equations which are discretised using FE.

Structural Matrices and Vectors in Finite Elements

In FE, the mass and stiffness matrices and the force vectors can be built by applying the Galerkin method on the weak formulation in equation (1.30) [4, 2]. The following matrices and vectors are now defined in a three-dimensional basis. Therefore, from now on, matrices and tensors will be

[2] Equations (1.27) to (1.29) are true $\forall m \in \Omega_s$ and $\forall t > 0$. Consequently, it will not be specified systematically at every equation

denoted with square brackets [] and vectors with squiggly brackets {}. The first term of the weak form provides the element mass matrix which reads:

$$[M_e] = \rho \int_{\Omega_e} [N]^T [N] dv \tag{1.31}$$

where $[N]$ is the element shape functions matrix and Ω_e is the element domain which is a volume. Note that, as opposed to equation (1.30), the density (ρ) has been taken out of the integral since it is constant for all the mechanical analyses in this project.

The second term of the weak form gives the element stiffness matrix which reads:

$$[K_e] = \int_{\Omega_e} [B]^T [D][B] dv \tag{1.32}$$

where $[B]$ is the strain displacement matrix based on the element shape functions and $[D]$ the elasticity tensor.

The third term of the weak form gives the element body force vector which reads:

$$\{F_e\} = \int_{\Omega_e} [N]^T \{F\} dv \tag{1.33}$$

Finally, the fourth term of the weak form gives the element traction, or surface, force vector which is:

$$\{t_{\mathrm{pe}}\} = \int_{\partial\Omega_e} [N_{\mathrm{n}}]^T \{t_{\mathrm{p}}\} ds \tag{1.34}$$

where $[N_{\mathrm{n}}]$ is the shape functions matrix for normal motion at the surface and $\partial\Omega_e$ the surface boundary of the element. In ANSYS Mechanical, the integrals are solved using Gauss numerical integration which is the most popular integration method in FE.

The total mass and stiffness matrices and the total force vectors read:

$$[M] = \sum_{e=1}^{N} [M_e] \tag{1.35}$$

$$[K] = \sum_{e=1}^{N} [K_e] \tag{1.36}$$

$$\{F\} = \sum_{e=1}^{N} \{F_e\} \tag{1.37}$$

where N is the total number of elements.

Steady State Analysis

In this work, steady state analyses of the test cases were computed to perform modal analyses in a prestressed environment. A steady state analysis solves for displacement, strain, and stress levels of a structure subjected to constant loads [7]. In a turbomachine, a rotor blade is subjected to three constant loads: thermal, centrifugal, and gaspath. On the other hand, a stator vane is subjected only to thermal and gaspath loads since it does not rotate.

The centrifugal load is a body force which reads:

$$\{F_{\mathrm{c}}\} = \rho \frac{\| \{\Omega_{\mathrm{R}}\} \times \{r\} \|^2}{\| \{r\} \|} \{\hat{e}_{\mathrm{r}}\} \tag{1.38}$$

where $\{\Omega_{\mathrm{R}}\}$ is the rotational velocity vector, $\{r\}$ the radial vector, and $\{\hat{e}_{\mathrm{r}}\}$ the unit vector in the radial direction. In the steady state analyses in this work, the radial vector is always perpendicular to the axis of rotation which is always parallel to the z axis.

Since it is a body force, the element centrifugal force vector can be computed using equation (1.33):

$$\{F_{\mathrm{c}e}\} = \int_{\Omega_e} [N]^T \{F_{\mathrm{c}}\} dv \tag{1.39}$$

The thermal load is another body force. During operation, temperature can reach up to a few hundreds of °C and, most of the time, is not distributed evenly in the blades or vanes. Therefore, the thermal strains induce a force which is called thermal load. the element thermal load vector reads:

$$\{F_{\mathrm{t}e}\} = \int_{\Omega_e} [B]^T [D] \{\epsilon_{\mathrm{t}e}\} dv \tag{1.40}$$

where $\epsilon_{\mathrm{t}e}$ is the element thermal strain matrix.

Finally, the gaspath load is the average aerodynamic pressure load at every location on the blade or vane surface. During operation, every location on blades and vanes surfaces is subjected to an aerodynamic pressure which is composed of a fluctuating term and an average term. The gaspath load is the average term. It has a considerable impact for steady stress assessments; however, the impact on the elasticity tensor ($[D]$), hence on prestress modal analyses results, is small. Consequently, the gaspath load was neglected.

In summary, for the steady state analyses of this project, the element force vector, which is the sum of the body force and traction force vectors, for a stator was:

$$\{F_e\} = \{F_{\mathrm{t}e}\} \tag{1.41}$$

and for a rotor:

$$\{F_e\} = \{F_{\mathrm{c}e}\} + \{F_{\mathrm{t}e}\} \tag{1.42}$$

The system of equations to solve for steady state analyses reads:

$$[K]\{u\} = \{F\} \tag{1.43}$$

where $\{u\}$ is the total displacement vector which is found by solving equation (1.43). The element strain vector can be computed in every element as follows:

$$\{\epsilon_e\} = [B]\{u_e\} \tag{1.44}$$

where $\{u_e\}$ is the element displacement vector. Finally, the stress vector can be computed in every element as follows:

$$\{\sigma_e\} = [D]\{\epsilon_e\} \tag{1.45}$$

The total strain and stress vectors can then be assembled:

$$\begin{aligned}\{\epsilon\} &= \sum_{e=1}^{N}\{\epsilon_e\} \\ \{\sigma\} &= \sum_{e=1}^{N}\{\sigma_e\}\end{aligned} \tag{1.46}$$

Modal Analysis

Modal analyses with prestress environment were performed on the test cases to find their steady natural linear sinusoidal frequencies and mode shapes and also to perform harmonic response analyses with the mode superposition method. With modal analyses in a prestress environment, the elasticity tensor ($[D]$) is linearized with respect to the steady state equilibrium induced by the constant loads. This equilibrium is solved with equation (1.43). This is why steady state analyses needed to be performed [7].

For a steady state modal analysis, the system of equations to solve is the following:

$$[M]\{\ddot{u}\} + [K]\{u\} = 0 \tag{1.47}$$

Note that the total stiffness matrix ($[K]$) has prestress effects included since it is computed with the linearized elasticity tensor ($[D]$). For linear sinusoidal free vibrations, the displacement vector ($\{u\}$) is known to be:

$$\{u\} = \{\phi_i\}\cos(\omega_{\mathrm{n}i}t) \tag{1.48}$$

where $\{\phi_i\}$ is the eigenvector of the ith mode shape and $\omega_{\mathrm{n}i}$ is the ith natural frequency. Substituting equation (1.48) into equation (1.47) yields:

$$(-\omega_{\mathrm{n}i}^2[M] + [K])\{\phi_i\} = \{0\} \tag{1.49}$$

Equation (1.49) is satisfied if $\{\phi_i\} = \{0\}$ or if the determinant of $[K] - \omega_{\mathrm{n}}^2[M]$ is zero. The first option being trivial is not of interest. The second option gives the following solution:

$$\det([K] - \omega_{\mathrm{n}}^2[M]) = 0 \tag{1.50}$$

This is an eigenvalue problem where the number of obtained ω_{n}^2 values is equal to the number of Degrees Of Freedom (DOF) of the system.

Once the $\omega_{\mathrm{n}i}^2$ values are obtained, the corresponding eigenvectors ($\{\phi_i\}$) and modal displacement vectors ($\{u\}$) for every mode can be computed. The modal strain vectors ($\{\epsilon\}$) and stress vectors ($\{\sigma\}$) for every mode can then be calculated using equations, (1.44), (1.45), and (1.46). Note that the only natural frequencies that are considered are the positive $\omega_{\mathrm{n}i}$ values since they are the only ones that have a physical meaning.

Transient Analysis

When performing a transient analysis, it can be assumed that the elasticity tensor ($[D]$) remains constant, meaning that the total stiffness matrix ($[K]$) is constant as well. This makes the elastic force vector ($\{F_{\text{el}}\}$) linearly proportional to the nodal displacement vector ($\{u\}$):

$$\{F_{\text{el}}\} = [K]\{u\} \tag{1.51}$$

In such a case, the system of equations becomes:

$$[M]\{\ddot{u}\} + [C]\{\dot{u}\} + [K]\{u\} = \{F(t)\} \tag{1.52}$$

In this work, the total damping matrix ($[C]$) was built using a given damping ratio (ζ) which is constant in space and time.

In transient analyses, the force vector ($\{F(t)\}$) is the sum of the thermal, centrifugal, and aerodynamic excitation loads. The system of equations is not linearized with respect to the steady state equilibrium induced by the constant loads because the ANSYS Mechanical software design does not allow it. If its design allowed such a transient analysis, the force vector would only have been the aerodynamic periodic excitation which is the only time dependent load, and the constant linearized elastic tensor ($[D]$) would have been used. Since the steady loads (thermal and centrifugal) have to be included in $\{F(t)\}$, the elastic tensor ($[D]$) cannot be considered as constant. Therefore, the elastic tensor ($[D]$) depends on the displacement vector ($\{u\}$). The system of equations to solve is therefore:

$$[M]\{\ddot{u}\} + [C]\{\dot{u}\} + \{F_{\text{el}}(\{u\})\} = \{F(t)\} \tag{1.53}$$

where:

$$\{F_{\text{el}}\} = [K(\{u\})]\{u\} \tag{1.54}$$

For solving this system of equations, the Newmark method is performed for solving the time domain [7]. Since this system of equations is nonlinear, any time integration operator is used in association with the Newton-Raphson algorithm. With the Newmark method, the system of equations at time t_{n+1} is:

$$[M]\{\ddot{u}_{n+1}\} + [C]\{\dot{u}_{n+1}\} + \{F_{\text{el}_{n+1}}\} = \{F_{n+1}\} \tag{1.55}$$

where:

$$\begin{aligned} \{F_{n+1}\} &= \{F_{n+1}(t_{n+1})\} \\ \{F_{\text{el}_{n+1}}\} &= \{F_{\text{el}_{n+1}}(\{u_{n+1}\}\} \end{aligned} \tag{1.56}$$

With the Newmark method, the position and velocity vectors at time t_{n+1} are:

$$\{u_{n+1}\} = \{u_n\} + \{\dot{u}_n\}\Delta t + \left[\left(\frac{1}{2} - \alpha\right)\{\ddot{u}_n\} + \alpha\{\ddot{u}_{n+1}\}\right]\Delta t^2 \tag{1.57}$$

$$\{\dot{u}_{n+1}\} = \{\dot{u}_n\}[(1-\delta)\{\ddot{u}_n\} + \delta\{\ddot{u}_{n+1}\}]\Delta t \tag{1.58}$$

where Δt is the time step size and α and δ the Newmark's integration parameters. By introducing a residual vector:

$$\{R_{n+1}\} = \{R_{n+1}(\{u_{n+1}\})\} \tag{1.59}$$

equation (1.55) becomes:

$$\{R_{n+1}\} = \{F_{n+1}\} - \{F_{\mathrm{el}_{n+1}}\} - [M]\{\ddot{u}_{n+1}\} - [C]\{\dot{u}_{n+1}\} \tag{1.60}$$

The linearized form of the integration operator is obtained using the Newton-Raphson algorithm as follows:

$$\{R_{n+1}\} + \frac{\partial\{R_{n+1}\}}{\partial\{u_{n+1}\}}\{\Delta u_{n+1,k}\} = \{0\} \tag{1.61}$$

with:

$$\{R_{n+1}\} = \{R_{n+1}(\{u_{n+1,k}\})\} \tag{1.62}$$

where $\{u_{n+1,k}\}$ is the estimate of $\{u_{n+1}\}$ at the kth residual convergence iteration and $\{\Delta u_{n+1,k}\}$ is the displacement increment of $\{u_{n+1}\}$ at the kth residual convergence iteration. Therefore, equation (1.55) linearized with the Newton-Raphson algorithm of equation (1.61) gives:

$$\Big[(a_0[M] + a_1[C]) + [K_{n+1}]\Big]\{\Delta u_{n+1,k}\} = \{R_{n+1}\} \tag{1.63}$$

where:

$$[K_{n+1}] = [K_{n+1}(\{u_{n+1,k}\})] \tag{1.64}$$

is the total stiffness matrix at time t_{n+1}, $\{R_{n+1}\}$ is as per equation (1.62), and:

$$a_0 = \frac{1}{\alpha\Delta t^2} \tag{1.65}$$

$$a_1 = \frac{\delta}{\alpha\Delta t} \tag{1.66}$$

With the Newmark method, the amount of numerical damping is controlled by the Newmark's integration parameters (α and δ). These parameters should respect the following conditions to have an unconditionally stable Newmark scheme:

$$\begin{aligned} \delta &\geq \frac{1}{2} \\ \alpha &\geq \frac{1}{4}\left(\frac{1}{2} + \delta\right)^2 \end{aligned} \tag{1.67}$$

In ANSYS Mechanical, an amplitude decaying factor (γ) is used to set the Newmark's integration parameters (α and δ) values. The relations between the Newmark's integration parameters and the amplitude decaying factor is:

$$\begin{aligned} \delta &= \frac{1}{2} + \gamma \\ \alpha &= \frac{1}{4}(1 + \gamma)^2 \end{aligned} \tag{1.68}$$

where:

$$\gamma \geq 0 \tag{1.69}$$

Note that the amplitude decaying factor (γ) satisfies the conditions given in equation (1.67). Increasing γ results, obviously, in increasing α and δ which results in increasing numerical damping and attenuating high frequency phenomena. In this work, transient analyses were performed to make a high frequency mode resonate. Accordingly, γ was set to zero for the transient analyses and the minimum acceptable α and δ values were used:

$$\begin{aligned} \delta &= \frac{1}{2} \\ \alpha &= \frac{1}{4} \end{aligned} \tag{1.70}$$

Harmonic Response Analysis

Harmonic response analyses solve the linear system in (1.52). As opposed to transient analyses, which can solve for any kind of time dependent external forces, harmonic response analyses can only be used under the following restrictions:

- The structure must have constant or frequency-dependent stiffness, damping, or mass effects.
- Loads and displacements must be sinusoidal and have the same known frequency, but may have different phases.
- Loads must not be complex except for pressures.

Since compressor blades and vanes receive periodic aerodynamic excitation, this method can be used for this project. Harmonic response analyses can be performed in a prestress environment just like modal analyses. Therefore, the system of equations in (1.52) can be linearized with respect to the equilibrium induced by the constant loads [7].

As stated above, every point in the structure is moving at the same known frequency. However, they may not have the same phase. It is also known that the presence of damping may cause phase shifts. The displacement vector can therefore be defined as:

$$\{u\} = \{u_{\mathrm{max}} \mathrm{e}^{\mathrm{i}\phi_{\mathrm{p}}}\} \mathrm{e}^{\mathrm{i}\Omega_{\mathrm{f}} t} \tag{1.71}$$

where $\mathrm{i} = \sqrt{-1}$, $\{u_{\mathrm{max}}\}$ is the maximum displacement vector, Ω_{f} the imposed, or forced, frequency, and ϕ_{p} the displacement phase. Similarly, the force vector is defined as:

$$\{F\} = \{F_{\mathrm{max}} \mathrm{e}^{\mathrm{i}\psi_{\mathrm{p}}}\} \mathrm{e}^{\mathrm{i}\Omega_{\mathrm{f}} t} \tag{1.72}$$

where $\{F_{\mathrm{max}}\}$ is the maximum force vector and ψ_{p} is the force phase.

If trigonometric notation is used, equations (1.71) and (1.72) become:

$$\{u\} = \{u_{\mathrm{max}}(\cos(\phi_{\mathrm{p}}) + \mathrm{i}\sin(\phi_{\mathrm{p}}))\} \mathrm{e}^{\mathrm{i}\Omega_{\mathrm{f}} t} \tag{1.73}$$

$$\{F\} = \{F_{\mathrm{max}}(\cos(\psi_{\mathrm{p}}) + \mathrm{i}\sin(\psi_{\mathrm{p}}))\} \mathrm{e}^{\mathrm{i}\Omega_{\mathrm{f}} t} \tag{1.74}$$

Furthermore, the following substitutions can be performed in these equations:

$$\{u\} = (\{u_1\} + \mathrm{i}\{u_2\}) \mathrm{e}^{\mathrm{i}\Omega_{\mathrm{f}} t} \tag{1.75}$$

$$\{F\} = (\{F_1\} + \mathrm{i}\{F_2\}) \mathrm{e}^{\mathrm{i}\Omega_{\mathrm{f}} t} \tag{1.76}$$

Therefore, substituting equations (1.75) and (1.76) into equation (1.52) yields:

$$([K] - \Omega_{\mathrm{f}}^2[M] + \mathrm{i}\Omega_{\mathrm{f}}[C])(\{u_1\} + \mathrm{i}\{u_2\})\mathrm{e}^{\mathrm{i}\Omega_{\mathrm{f}}t} = (\{F_1\} + \mathrm{i}\{F_2\})\mathrm{e}^{\mathrm{i}\Omega_{\mathrm{f}}t} \tag{1.77}$$

Dividing the above system of equations by $\mathrm{e}^{\mathrm{i}\Omega_{\mathrm{f}}t}$ leads to:

$$([K] - \Omega_{\mathrm{f}}^2[M] + \mathrm{i}\Omega_{\mathrm{f}}[C])(\{u_1\} + \mathrm{i}\{u_2\}) = \{F_1\} + \mathrm{i}\{F_2\} \tag{1.78}$$

Equation (1.78) gives the system of equations that is solved in harmonic response analyses. For solving it, the two most popular methods are the full solution and the mode superposition methods. With the full solution method, the system of equations is solved with Gaussian elimination via complex algebra.

On the other hand, the mode superposition method uses the natural frequencies and mode shapes obtained from modal analysis to calculate the response. Using this method imposes two extra restrictions:

- Nonzero imposed harmonic displacements are not permitted
- Element damping matrices are not permitted

In this work, no nonzero harmonic displacements were imposed and the damping was always given as a constant damping ratio (ζ) independent of space or frequency. Therefore, the two restrictions are satisfied and the mode superposition method was used for all the harmonic response analyses. It is important to note that, with this method, the total force vector ($\{F\}$) reads:

$$\{F\} = \{F_{\mathrm{nd}}\} + s\{F_{\mathrm{s}}\} \tag{1.79}$$

where $\{F_{\mathrm{nd}}\}$ is the imposed sinusoidal force, $\{F_{\mathrm{s}}\}$ the load vector computed from the modal analysis, and s the load vector scale factor.

The first step for employing the mode superposition method is to go back to the system of equations in (1.52) and convert it to modal form. The following set of modal coordinates (y_{i}) is first defined:

$$\{u\} = \sum_{i=1}^{n}\{\phi_i\}y_i \tag{1.80}$$

where $\{\phi_i\}$ is the ith mode shape vector and n is the total number of modes to be used. Substituting the above equation in equation (1.52) gives:

$$[M]\sum_{i=1}^{n}\{\phi_i\}\ddot{y}_i + [C]\sum_{i=1}^{n}\{\phi_i\}\dot{y}_i + [K]\sum_{i=1}^{n}\{\phi_i\}y_i = \{F\} \tag{1.81}$$

Premultiplying the above equation by the transpose of any typical mode shape vector $\{\phi_j\}^T$ gives:

$$\{\phi_j\}^T[M]\sum_{i=1}^{n}\{\phi_i\}\ddot{y}_i + \{\phi_j\}^T[C]\sum_{i=1}^{n}\{\phi_i\}\dot{y}_i + \{\phi_j\}^T[K]\sum_{i=1}^{n}\{\phi_i\}y_i = \{\phi_j\}^T\{F\} \tag{1.82}$$

The orthogonal condition of the natural modes states the following:

$$\begin{aligned}\{\phi_j\}^T[M]\{\phi_i\} &= 0, \quad \forall i \neq j\\ \{\phi_j\}^T[K]\{\phi_i\} &= 0, \quad \forall i \neq j\end{aligned} \tag{1.83}$$

As stated above, element damping matrices are not permitted with the mode superposition method. The damping is given as a Rayleigh (mass and stiffness matrix coefficients α and β) or constant damping factor (ζ). In the mode superposition method, the damping is such that:

$$\{\phi_j\}^T[C]\{\phi_i\} = 0, \quad \forall i \neq j \tag{1.84}$$

The damping was given as a constant damping ratio (ζ) for all the harmonic response analyses performed in this project.

Applying the conditions of equations (1.83) and (1.84), only the $i = j$ terms of equation (1.82) remain which gives:

$$\{\phi_j\}^T[M]\{\phi_j\}\ddot{y}_j + \{\phi_j\}^T[C]\{\phi_j\}\dot{y}_j + \{\phi_j\}^T[K]\{\phi_j\}y_j = \{\phi_j\}^T\{F\} \tag{1.85}$$

In ANSYS Mechanical, it is imposed that the $\ddot{y}_j$ coefficient is unity:

$$\{\phi_j\}^T[M]\{\phi_j\} = 1 \tag{1.86}$$

This is the normality condition when each eigenvector is normalized to the mass matrix.

The damping term is based on treating the modal coordinate as a single DOF system. Accordingly, the $\dot{y}_j$ coefficient becomes:

$$\{\phi_j\}^T[C]\{\phi_j\} = C_j\phi_j^2 \tag{1.87}$$

In this work, C_j is actually the same for every mode since a constant damping ratio (ζ) is provided in every performed harmonic analysis. For a single DOF system, damping (C_j) can be expressed in terms of damping ratio (ζ_j) as follows:

$$C_j = 2\zeta_j\sqrt{K_jM_j} \tag{1.88}$$

The mass term is also based on treating the modal coordinate as a single DOF system and the $\ddot{y}_j$ coefficient becomes:

$$\{\phi_j\}^T[M]\{\phi_j\} = M_j\phi_j^2 \tag{1.89}$$

However, from equation (1.86), equation (1.89) yields:

$$M_j\phi_j^2 = 1 \tag{1.90}$$

where solving for ϕ_j implies:

$$\phi_j = \frac{1}{\sqrt{M_j}} \tag{1.91}$$

In single DOF, the natural frequency of the jth mode is:

$$\omega_{\mathrm{n}j} = \sqrt{\frac{K_j}{M_j}} \tag{1.92}$$

Therefore, substituting equations (1.88), (1.91), and (1.92) into equation (1.87) gives:

$$\{\phi_j\}^T[C]\{\phi_j\} = 2\zeta_j\sqrt{K_jM_j}\left(\frac{1}{\sqrt{M_j}}\right)^2 = 2\zeta_j\omega_{\mathrm{n}j} \tag{1.93}$$

From equation (1.49), it can be stated that:

$$[K]\{\phi_j\} = \omega_{\mathrm{n}j}^2[M]\{\phi_j\} \tag{1.94}$$

Premultiplying by $\{\phi_j\}^T$ gives:

$$\{\phi_j\}^T[K]\{\phi_j\} = \omega_{\mathrm{n}j}^2\{\phi_j\}^T[M]\{\phi_j\} \tag{1.95}$$

and utilizing equation (1.86) gives:

$$\{\phi_j\}^T[K]\{\phi_j\} = \omega_{\mathrm{n}j}^2 \tag{1.96}$$

For convenience, the following notation is introduced:

$$f_j = \{\phi_j\}^T\{F\} \tag{1.97}$$

Substituting equations (1.86), (1.93), (1.96), and (1.97) into equation (1.85) gives the equations of motion in modal coordinates which reads:

$$\ddot{y}_j + 2\omega_{\mathrm{n}j}\zeta_j\dot{y}_j + \omega_{\mathrm{n}j}^2y_j = f_j \tag{1.98}$$

For a steady sinusoidal vibration, f_j and y_j must be of the form:

$$f_j = f_{\mathrm{c}j}\mathrm{e}^{\mathrm{i}\Omega_{\mathrm{f}}t} \tag{1.99}$$

$$y_j = y_{\mathrm{c}j}\mathrm{e}^{\mathrm{i}\Omega_{\mathrm{f}}t} \tag{1.100}$$

where $f_{\mathrm{c}j}$ is the complex force, $y_{\mathrm{c}j}$ the complex amplitude of the jth mode, and, as specified earlier, Ω_{f} the imposed, or forced, frequency.

Substituting equations (1.99) and (1.100) into equation (1.98) gives:

$$-\Omega_{\mathrm{f}}^2y_{\mathrm{c}j}\mathrm{e}^{\mathrm{i}\Omega_{\mathrm{f}}t} + 2\omega_{\mathrm{n}j}\zeta_j\mathrm{i}\Omega_{\mathrm{f}}y_{\mathrm{c}j}\mathrm{e}^{\mathrm{i}\Omega_{\mathrm{f}}t} + \omega_{\mathrm{n}j}^2y_{\mathrm{c}j}\mathrm{e}^{\mathrm{i}\Omega_{\mathrm{f}}t} = f_{\mathrm{c}j}\mathrm{e}^{\mathrm{i}\Omega_{\mathrm{f}}t} \tag{1.101}$$

Dividing by $\mathrm{e}^{\mathrm{i}\Omega_{\mathrm{f}}t}$ and putting $y_{\mathrm{c}j}$ in evidence, the expression:

$$(-\Omega_{\mathrm{f}}^2 + 2\omega_{\mathrm{n}j}\zeta_j\mathrm{i}\Omega_{\mathrm{f}} + \omega_{\mathrm{n}j}^2)y_{\mathrm{c}j} = f_{\mathrm{c}j} \tag{1.102}$$

is obtained. Solving for $y_{\mathrm{c}j}$ gives:

$$y_{\mathrm{c}j} = \frac{f_{\mathrm{c}j}}{(\omega_{\mathrm{n}j}^2 - \Omega_{\mathrm{f}}^2) + \mathrm{i}(2\omega_{\mathrm{n}j}\Omega_{\mathrm{f}}\zeta_j)} \tag{1.103}$$

The contribution vector from each mode ($\{C_j\}$) can then be computed as follows:

$$\{C_j\} = \{\phi_j\}y_{\mathrm{c}j} \tag{1.104}$$

Finally, the complex displacement vector ($\{u_c\}$) is:

$$\{u_c\} = \sum_{j=1}^{n} \{C_j\} \tag{1.105}$$

Strain and stress vectors can then be calculated using equations (1.44), (1.45), and (1.46).

The advantage of working with the mode superposition method is that the system of equations in modal coordinates is uncoupled. This is because all the matrix algebra is solved in the modal analysis and this is what requires the most computational effort and time. Usually, before performing a harmonic response analysis, performing a modal analysis is good engineering practice since knowing the natural frequencies and mode shapes of a structure tells a lot about its dynamic behaviour. However, particular attention must be paid to the number of modes that is considered when using the method. If too few modes are considered, results may not be accurate and meaningful.

1.2.3 Coupling Types

In static and dynamic aeroelasticity theory, there exists some closed-form solution for simple case problems. However, when it comes to solving for complex geometries subjected to complex aerodynamic loads such as those in this work, FE and CFD numerical tools built as per the equations presented in sections 1.2.1 and 1.2.2 shall be employed. For solving an aeroelasticity problem with these numerical tools, a coupling method of the FE and CFD solvers must be chosen. The possible solution methods are shown in figure 1.6.

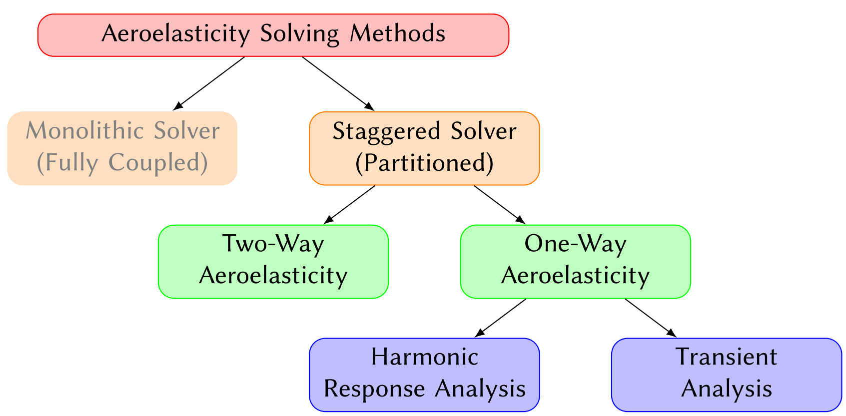

Figure 1.6: Aeroelasticity solvers used in this project

When solving complex three dimensional problems like the ones solved in industry like P&WC, staggered solvers are used. A staggered solver is actually a combination of a FE solver and a CFD solver which are both fully independent in nature [8]. In other words, they are often used independently for solving dynamic aerodynamics or dynamic solid mechanics problems. When doing aeroelasticity, the CFD solver handles the fluid related calculation and the FE solver handles solid related calculation. The two solvers exchange information at their fluid-solid interface ($\partial\Omega_{fsi}$) so that the effects of the fluid on the solid can be considered and vice versa. Since two solvers are involved, a non-conformal mesh of the fluid and the solid domain can be used. A non-conformal mesh means that the nodes of the two meshes do not share the same coordinates at $\partial\Omega_{\text{fsi}}$. A two dimensional non-conformal mesh example is shown in figure 1.7a. Further details on staggered solver will be given in the coming sections.

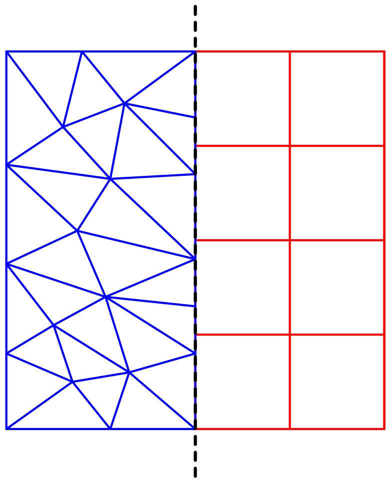

(a) Non-conformal mesh

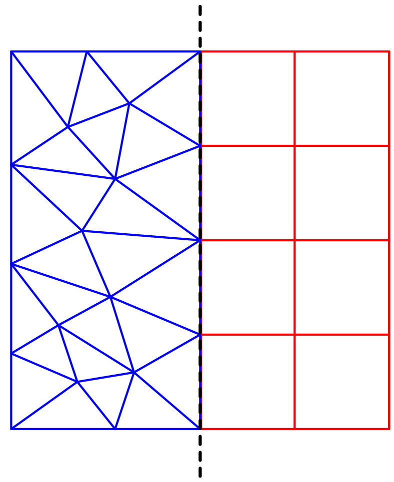

(b) Conformal mesh

Figure 1.7: Fluid-structure meshes: structure (—) and fluid (—)

On the other hand, an aeroelasticity monolithic solver is a single solver resolving the equations of the fluid and the solid simultaneously. The fluid and solid equations are therefore discretised and solved together. This requires a conformal mesh with matching nodal positions between the solid and the fluid meshes. A conformal mesh means that the nodes of the two meshes share the same coordinate at $\partial\Omega_{\text{fsi}}$. A two dimensional conformal mesh example is shown in figure 1.7b. Even though this type of solver is the most robust, it is not used yet in numerical commercial tools such as ANSYS.

1.2.4 One-Way Aeroelasticity

When solving aeroelasticity problems using a staggered approach, it can be decided to consider only the aerodynamic forces subjected to the body without considering the solid displacements in the fluid domain. This reduces considerably the complexity of the analysis and the required computational power. The CFD portion is first solved in standalone, the aerodynamic forces on the fluid-solid interface ($\partial\Omega_{\text{fsi}}$) are extracted and applied on the solid domain. Then, the FE analysis portion is solved. Therefore, the only exchange of information that occurs at the fluid-solid interface ($\partial\Omega_{\text{fsi}}$) is the aerodynamic forces transferred from the CFD solver to the FE solver. There is no mesh morphing in the fluid domain since the solid domain is rigid when the CFD portion is being solved. This type of analysis is called one-way aeroelasticity. One-way aeroelasticity analysis is one of the two kinds of analysis that can be done using a staggered solver as shown in figure 1.6.

In dynamic aeroelasticity, if accurate results are desired, the one-way aeroelasticity assumption may be used only if certain conditions are respected. First, one-way aeroelasticity shall not be used if an asynchronous response, for instance flutter, is expected in reality. One-way aeroelasticity cannot predict such responses since the energy added to or removed from the solid by the fluid is not captured, as the CFD solver does not consider the solid mesh displacements. Second, the displacements of the solid domain must be small compared to the size of the fluid domain. If the displacements of the solid domain are too large compared to the fluid domain size, the analysis results will not be accurate. Finally, an accurate value of the aerodynamic damping must be known and imposed in the FE analysis. This is particularly important when the synchronous response of a mode in resonance is analyzed as performed in this project.

As stated above, the first step in one-way aeroelasticity analysis is to perform the CFD. In dynamic aeroelasticity, a transient CFD analysis is required. However, a good industrial practice in aerodynamics is to perform steady CFD analyses first. It is recommended to ensure that the mesh size is appropriate for the averaged flow quantities and that no mistakes have been made in the analysis setup. As explained in section 1.2.1, in this project, the steady analyses were performed using the time independent RANS equations using the mixing plane concept. Once it is demonstrated that the steady CFD analyses converge properly and that the mesh density is acceptable, the transient CFD analyses can be conducted.

As stated as well in section 1.2.1, the transient analyses were done using the full RANS equations with the TBR method. Once the transient CFD analyses are completed, the static pressure ($p_\mathrm{s} = p_\mathrm{s}(x, y, z, t)$) should be extracted $\forall t$ and $\forall x, y, z \in \partial\Omega_\mathrm{fsi}$. With the extracted static pressure, the FE analysis of the solid can be conducted.

As shown in figure 1.6, there exist two kinds of one-way aeroelasticity analyses: transient and harmonic response analyses. From an aerodynamics (or CFD) point of view, there is no difference between a transient and harmonic response one-way aeroelasticity analysis. The fact that the one-way aeroelasticity analysis is a transient or harmonic response one depends only on the type of FE analysis that is performed using the static pressure extracted from the transient CFD analysis.

The details and theory about transient and harmonic response FE analyses were presented in section 1.2.2. Since the time domain is solved in a transient analysis, it requires much more computational power and time than a harmonic response analysis. If the transient phenomenon of interest is not periodic, then a transient analysis is required. On the other hand, if the dynamic behaviour of the structure is only needed for specific periodic excitation, a harmonic analysis should be performed to save computational power and time.

If transient one-way aeroelasticity is chosen, the extracted static pressure from the transient CFD analysis must be mapped on the solid mesh nodes belonging to $\partial\Omega_\mathrm{fsi}$ by fixed-point iteration. With this pressure mapping on $\partial\Omega_\mathrm{fsi}$, the traction or force vector ($\{t_\mathrm{p}\}$) can be computed. Then, using equations (1.34), (1.41) or (1.42), and (1.37), the total force vector ($\{F\} = \{F(t)\}$) can be constructed. The system of equations (1.53) can then be solved as per the FE transient analysis method detailed in section 1.2.2.

On the other hand, if harmonic response one-way aeroelasticity is chosen, Fast Fourier Transform (FFT) is performed on the static pressure extracted from the transient CFD analysis and the real and imaginary static pressures (p_real and p_imag) corresponding to the desired imposed or forced frequency (Ω_f) are computed. Therefore, the complex pressure on the fluid-solid interface ($\partial\Omega_\mathrm{fsi}$) reads:

$$p_{\mathrm{c}j} = p_{\mathrm{c}j}(x, y, z) = p_{\mathrm{real}j}(x, y, z) + \mathrm{i}p_{\mathrm{imag}j}(x, y, z), \quad \forall x, y, z \in \partial\Omega_\mathrm{fsi} \tag{1.106}$$

The complex pressure is then mapped on every solid mesh node belonging to $\partial\Omega_{\mathrm{fsi}}$ by fixed-point iteration. The complex force (f_{cj}) can then be computed. The harmonic response analysis with the mode superposition method can then be performed by solving equations (1.103) to (1.105).

1.2.5 Two-Way Aeroelasticity

If an asynchronous response of the solid is expected, for instance flutter, or if the solid displacements are large compared to the size of the fluid domain, a one-way aeroelasticity analysis would not give meaningful results. In these circumstances, a two-way aeroelasticity analysis should be performed instead. In dynamic two-way aeroelasticity, the transient CFD and FE analyses must be solved simultaneously and exchange information at every time step at the fluid-solid interface ($\partial\Omega_{\mathrm{fsi}}$) by fixed-point iteration. A harmonic response is not possible with ANSYS.

In the two-way aeroelasticity analysis attempted in this project, it has been decided to solve the solid domain first at every time step. Therefore, at the beginning of time step t_n, the system of equations (1.53) is solved using the FE transient analysis methodology described in section 1.2.2. Once it is solved, the following BCs are imposed:

$$\begin{aligned} \{u_{\mathrm{fsi,f}}\}(t_n) &= \{u_{\mathrm{fsi,s}}\}(t_n) \\ \{\dot{u}_{\mathrm{fsi,f}}\}(t_n) &= \{\dot{u}_{\mathrm{fsi,s}}\}(t_n) \end{aligned} \tag{1.107}$$

where $\{u_{\mathrm{fsi,f}}\}$ and $\{u_{\mathrm{fsi,s}}\}$ are the displacement vectors at the fluid-structure interface of the fluid and solid domains respectively and $\{\dot{u}_{\mathrm{fsi,f}}\}$ and $\{\dot{u}_{\mathrm{fsi,s}}\}$ are the velocity vectors at the fluid-structure interface of the fluid and solid domains respectively. These quantities are mapped from the solid domain to the fluid domain by fixed-point iteration and they induce deformation of the mesh of the fluid domain. The time dependent RANS equations presented in section 1.2.1 can then be solved at t_n.

Once the RANS equations have been solved for this time step (t_n), the following BC is imposed:

$$p_{s_{\mathrm{fsi,s}}}(t_{n+1}) = p_{s_{\mathrm{fsi,f}}}(t_n) \tag{1.108}$$

where $p_{s_{\mathrm{fsi,s}}}$ and $p_{s_{\mathrm{fsi,f}}}$ the static pressures at the fluid-structure interface on the solid and fluid domains respectively. With this static pressure mapping on the solid domain on $\partial\Omega_{\mathrm{fsi}}$ by fixed-point iteration, the traction force vector $\{t_p\}$ and the total force vector $\{F\}$ can be computed at t_{n+1} and the iterative time integration process can continue. The CFD solver also calculates the aerodynamic damping at t_n so that the FE solver can use it for t_{n+1}.

In CFX, the TBR method does not support mesh morphing and therefore cannot be used. The two-way aeroelasticity analysis attempt was therefore undertaken using the pitch scaling approach detailed in section 1.2.1 and illustrated in figure 1.3.

1.3 Test Cases

Two test cases were chosen for establishing the dynamic aeroelasticity procedure: the compressor rotor 2 blade of a PT6 turboshaft engine and the compressor stator 1 vane of a PT6 turbopropeller engine. A simplified cross-section of the PT6 engine in shown in figure 1.8. This simplified cross section is valid for both the turboshaft and turbopropeller versions of the PT6 engine.

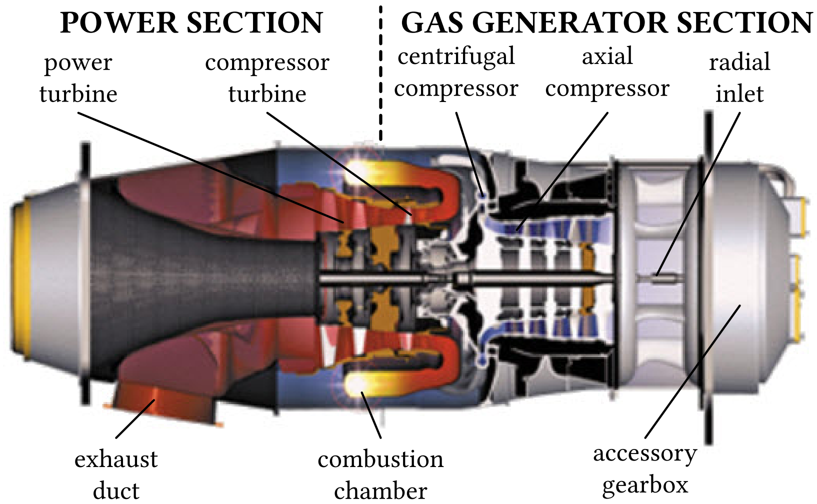

Figure 1.8: PT6 engine simplified cross-section

The PT6 turboshaft engines can develop 1,000 to 2,000 shaft horsepower and the PT6 turbo-propeller engines 500 to 2,000 shaft horsepower depending on aircraft and costumer applications. Every PT6 engine is composed of a radial inlet, a four-stage axial compressor, a single-stage centrifugal compressor (an impeller), and a three-stage turbine. It is a two-spool engine. Every compressor rotor and the first turbine stage rotor are mounted on the shaft named the gas generator shaft or Ng. The turbine second and third stage rotors are mounted on the other shaft named the Power Turbine (PT) shaft or Npt. The Npt shaft is the one connected to the aircraft gearbox hence providing the power. The Ng shaft on the other hand provides the necessary gas flow to turn the Npt shaft.

1.3.1 PT6 Turboshaft Compressor Rotor 2 Blade

The first test case is the compressor rotor 2 blade of a PT6 turboshaft engine application. This rotor is a 25 blade Integrated Bladed Rotor (IBR) for this turboshaft application and it is located between stators 1 and 2 as shown in figure: 1.9. In this project, the vibratory stress levels induced by the periodic excitation from stator 1 were studied. This excitation is an upstream excitation which means that it is caused by the periodic wakes of the stator 1 vanes. As shown in figure 1.9, stator 1 is composed of 40 vanes for this turboshaft application.

The rotor 2 model used in the FE analyses is shown in figure 1.10. This model is actually a 14.4° (1/25) sector of the full 360° rotor. The reasons why only a 14.4° sector was used will be explained in section 2.2.

1.3.2 PT6 Turbopropeller Compressor Stator 1 Vane

The second test case is the compressor stator 1 vane of a PT6 turbopropeller application. On the application in question, the stator 1 is composed of 40 vanes brazed on a shroud as shown in figure 1.11 and it is located between rotors 1 and 2. In this project, the vibratory stress levels induced by the periodic excitation from rotor 1 were studied. This excitation is an upstream excitation which

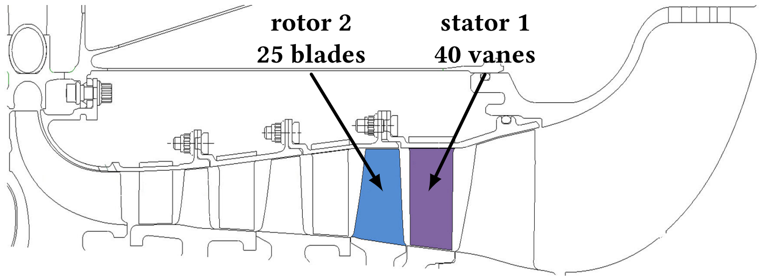

Figure 1.9: PT6 turboshaft compressor cross-section

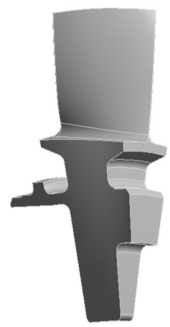

Figure 1.10: Rotor 2 sector

means that it is caused by the periodic wakes of the rotor 1 blades.

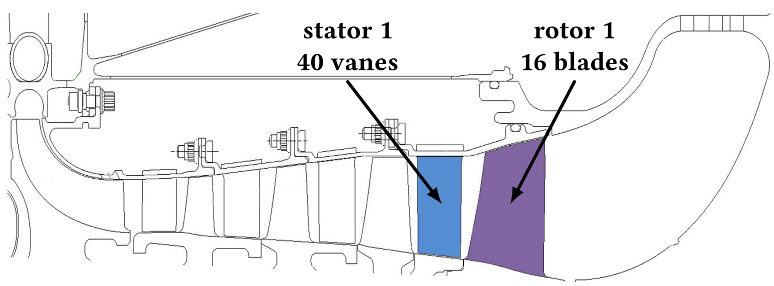

Figure 1.11: PT6 turboshaft compressor cross-section

One of the stator 1 models used in the FE analyses is shown in figure 1.12. This model is a 27° (3/40) sector of the full 360° stator. The other model used in the FE analyses is the full 360° model. The reasons why FE analyses were done with these models will be explained in section 3.2.

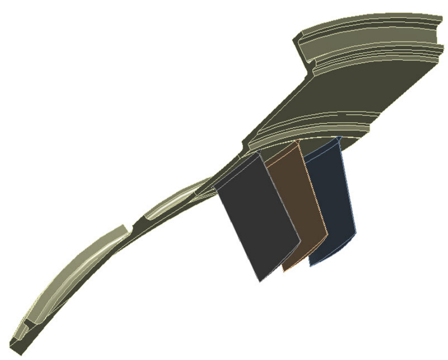

Figure 1.12: Stator 1 sector

Chapter 2

Aeroelasticity Analyses on PT6 Turboshaft Compressor Rotor 2 Blade

2.1 Strain Gauge Test Results Review

Before taking a look at vibratory stress data of rotor 2, the potential aerodynamic periodic excitation sources must be known. As explained in section 1.3, every rotor in the compressor is mounted on the Ng shaft in PT6 engines. Therefore, the relative velocity between a rotor blade and another rotor blade is zero. Accordingly, the rotor 2 blades cannot receive aerodynamic periodic excitation from the blades of another rotor. The components that can induce considerable excitation to the rotor 2 are the stators. Since they are stationary, the relative velocity between every stator vane and the rotor 2 blades is the absolute velocity of the Ng shaft which will be named Ω_{Ng}.

Any stator aerodynamic periodic excitation frequency (Ω_{fS}) is:

$$\Omega_{\mathrm{fS}} = N_{\mathrm{v}} \Omega_{\mathrm{Ng}} \tag{2.1}$$

where N_{v} is the number of vanes of the stator. Furthermore, the Engine Order (EO) of a stator aerodynamic periodic excitation is defined as:

$$E_{\mathrm{O}} = N_{\mathrm{v}} = \frac{\Omega_{\mathrm{fs}}}{\Omega_{\mathrm{Ng}}} \tag{2.2}$$

When rotor 2 has a mode in resonance, calculating the EO indicates which stator is the source of excitation.

For the case of this PT6 turboshaft compressor, when rotor 2 was experiencing its highest vibratory stress during the test, the EO was equal to 40. Since the EO depends on the rotational velocity of the Ng shaft, this excitation will be denoted as a 40ENg excitation. The stator 1 could therefore be identified as the excitation source since it is composed of 40 vanes. It makes a lot of sense that the highest vibratory stress was caused by the stator 1 excitation because in an axial compressor, the upstream adjacent component is the one inducing the highest excitation. The waterfall plot in figure 2.1 shows the highest vibratory stress recorded.

In this waterfall plot, σ is the vibratory stress axis, Ω_{f} the frequency axis, and Ω_{Ng} the Ng shaft rotational velocity axis. The red line represents the 40ENg line and the following is true for every point on this line:

$$\frac{\Omega_{\mathrm{f}}}{\Omega_{\mathrm{Ng}}} = 40 \tag{2.3}$$

The highest vibratory stress measured by the strain gauge is also shown on the waterfall plot. This stress will be called $\sigma_{\mathrm{R2,sg}}$. The green and orange lines crossing $\sigma_{\mathrm{R2,sg}}$ are, respectively, the vibratory stress frequency ($\Omega_{\mathrm{fS1,sg}}$) and the Ng rotational speed ($\Omega_{\mathrm{R2,sg}}$) for which $\sigma_{\mathrm{R2,sg}}$ occurs.

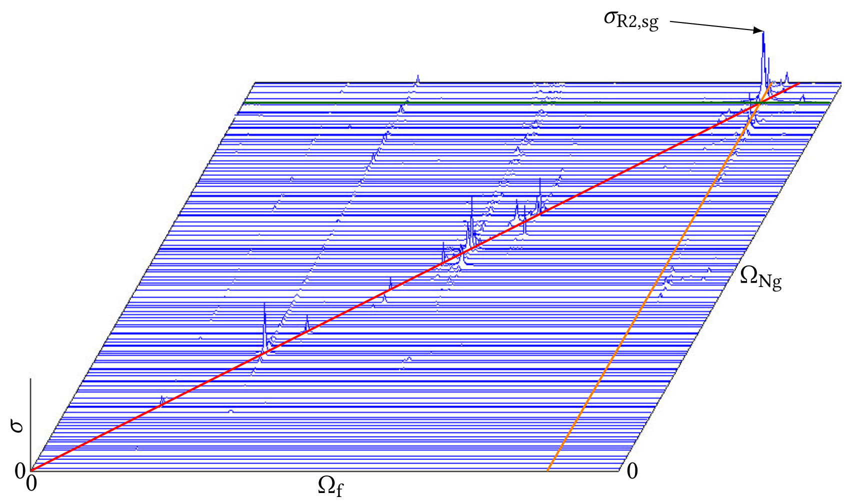

Figure 2.1: Waterfall plot: strain gauge data (—), 40ENg (—), $\Omega_{fS1,sg}$ (—), and $\Omega_{R2,sg}$ (—)

Note that the 40ENg line is crossing $\sigma_{R2,sg}$ indicating that this stress was a 40ENg one meaning that it was caused by a 40ENg excitation, hence stator 1. Finally, it can also be observed that other resonances due to the stator 1 excitation occur at lower frequencies since other vibratory stress peaks were present. However, $\sigma_{R2,sg}$ was the highest measured vibratory stress. To make a better assessment of all the 40ENg vibratory stress peaks amplitudes, the 40ENg plot shown in figure 2.2 was generated.

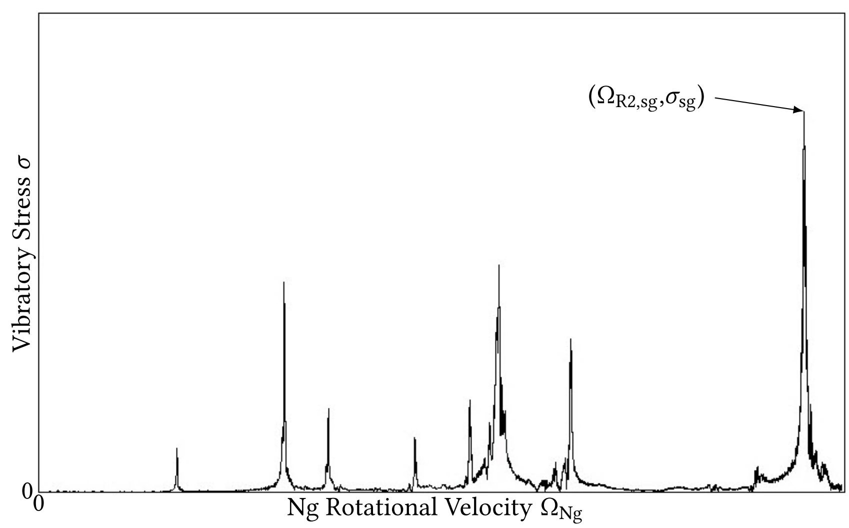

Figure 2.2: 40ENg plot: 40ENg strain gauge data (—)

On this 40ENg plot, only the 40ENg vibratory stress is considered and plotted with respect to Ω_{Ng}. All the 40ENg vibratory stress peaks featuring on the waterfall plot in figure 2.1 are shown in the 40ENg plot as well, but a much better assessment of their amplitudes can be achieved. It can then be observed that $\sigma_{R2,sg}$ was at least twice higher than any other 40ENg vibratory stress peak. This resonance was therefore an excellent candidate for testing the aeroelasticity procedure.

2.2 Modal Analysis

Before performing the modal analysis, the Nodal Diameter (ND) in resonance when the rotor 2 receives a 40ENg excitation was calculated. On an IBR composed of an axisymmetric disk and identical equally spaced blades such as rotor 2, the modal displacement and modal stress levels are the same on every blade for any mode shape. However, the blades do not necessarily vibrate in phase. This is where the notion of ND is important.

For an IBR or any bladed disk, the ND is an integer stating the number of times that a full mode shape cycle repeats itself on the full circumference. If the number of blades (N_b) is even, the possible NDs are:

$$0 \leq N_\mathrm{D} \leq \frac{N_\mathrm{b}}{2} \tag{2.4}$$

and if the number of blades is odd, the possible NDs are:

$$0 \leq N_\mathrm{D} \leq \frac{N_\mathrm{b} - 1}{2} \tag{2.5}$$

An ND 0 means that all the blades are in phase in a given mode shape. Note as well that the modes have different natural frequencies for every ND.

The ND in resonance on a bladed rotor is found by aliasing as follows:

$$N_\mathrm{D} = -E_\mathrm{O} + n_\mathrm{i} N_\mathrm{b} \tag{2.6}$$

where n_i is any positive integer or zero. Note that with this equation, negative and positive N_D values can be obtained. A negative value means that the modes travel in the opposite direction to the shaft rotation and a positive value means that the modes travel in the same direction as the shaft rotation for the ND in question. A mode travelling in the opposite direction of shaft rotation will be denoted as a backward travelling wave and a mode travelling in the same direction as the shaft rotation as a forward travelling wave.

Rotor 2 has 25 blades and was subjected to a 40ENg excitation from stator 1. As per equation (2.5), the highest possible ND is 12. Moreover, as per equation (2.6), the ND in resonance is 10, forward travelling wave. Therefore, the $\sigma_{R2,sg}$ stress obtained in the strain gauge test was from a mode in resonance at ND 10.

As stated in section 2.1, the rotor 2 model is a 14.4° (1/25) sector of the full 360° model. Since harmonic response and transient one-way aeroelasticity and two-way aeroelasticity analyses were desired, cyclic conditions could not be imposed since the aerodynamic forces applied on one blade are not cyclic. Moreover, even though the forces were cyclic, the ANSYS version being used does not support cyclic conditions in harmonic and transient analyses.

The reason why it has been decided to use a 1/40 sector without using cyclic conditions rather than the full 360° model is that the ND in resonance was near the maximum ND (10 vs. 12). Therefore, the disk was almost acting like a rigid body for such a high ND. This model was therefore meshed for performing the modal analysis and the FE portions of the aeroelasticity analyses. The rotor 2 mesh of the blade is shown in figure 2.3.

Figure 2.3: Blade mesh of the rotor 2

The clamped BCs applied on the model are shown in figure 2.4. In terms of FE, the clamped BCs mean that:

$$\{u\} = 0, \quad \forall x, y, z \in \partial\Omega_{\mathrm{BC}} \tag{2.7}$$

where $\partial\Omega_{\mathrm{BC}}$ is any surface where the clamped BCs are applied. Therefore, the FE model that was analyzed can be summarized as follows:

- Mesh composed of quadratic tetrahedron elements
- 525,992 nodes
- 305,448 elements
- 1,577,976 DOF on the complete model
- 17,788 nodes affected by the clamped BCs
- 1,524,612 DOF for the reduced model due to BCs

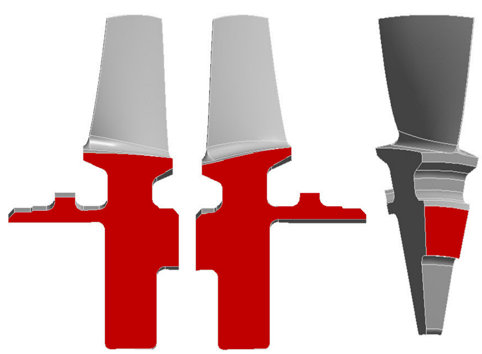

Figure 2.4: Rotor 2 clamped BCs

As explained in section 1.2.2 the modal analysis of rotor 2 was performed in a prestress environment. Accordingly, a steady state analysis, which calculates the equilibrium induced by the constant loads, was performed. With these results, the elasticity tensor ($[D]$) was linearized with respect to this equilibrium and the total stiffness matrix ($[K]$) was rebuilt. The steady loads to consider were the centrifugal and thermal loads. During the strain gauge test, $\sigma_{R2,sg}$ occurred at the rotational velocity of $\Omega_{R2,sg}$. The steady state analysis was therefore performed using this rotational velocity and the temperature distribution on rotor 2 at this rotational velocity.

The modal analysis was then performed by solving the system of equations (1.50) and the natural frequencies, modal deflection, strain, and stress levels were calculated. Mode 14 was identified as the closest frequency to $\Omega_{fS1,sg}$. This was the mode in resonance during the strain gauge test. The calculated natural frequency of mode 14 will be denoted as ω_{R2}. The calculated natural frequency was found to be 3.35% lower than the frequency at which it was in resonance during strain gauge test:

$$\omega_{R2} = 0.9665\Omega_{fS1,sg} \tag{2.8}$$

which is an acceptable error. The mode shape of mode 14 is shown in the modal displacement levels plot in figure 2.5. As can be observed, the modal displacement levels of this mode shape are concentrated at the tip of the blade.

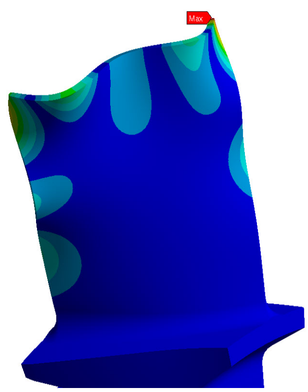

Figure 2.5: Rotor 2 mode shape of mode 14

The σ_{11} and σ_{33} stress distributions were both looked at. The highest stress found is shown in the stress distribution of the suction side of the blade in figure 2.6. This highest stress was located at the tip near the leading edge. The highest stress location is called the critical location. Every numerical vs. experimental comparison were done at the critical location.

The strain gauge that measured $\sigma_{R2,sg}$ was not located at the critical location. Therefore, a stress scaling factor (S_F) was calculated using the stress distribution of mode 14. The stress value at the critical location ($\sigma_{R2,cl}$) was:

$$\sigma_{R2,cl} = S_F\sigma_{R2,sg} \tag{2.9}$$

when $\sigma_{R2,sg}$ was measured.

To make sure that these modal analysis results were representative of reality when mode 14 was in resonance at ND 10, the modal analysis was launched again using cyclic conditions on the sector for comparison purposes only. As mentioned before, the model with cyclic conditions cannot be used in the aeroelasticity analyses. The clamped BCs on the 2 left images in figure 2.4 were therefore replaced by cyclic conditions. The BCs for this cyclic modal analysis are shown in

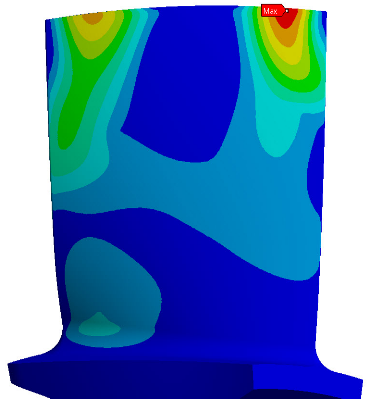

Figure 2.6: Rotor 2 σ_{11} stress distribution on the suction side for mode 14

figure 2.7. The calculated natural frequency for mode 14, ND 10, was 1.63% higher than the one obtained without cyclic symmetry and therefore 1.72% lower than during the strain gauge test:

$$\begin{aligned} \omega_{\mathrm{R2,c}} &= 1.0163\omega_{\mathrm{R2}} \\ \omega_{\mathrm{R2,c}} &= 0.9828\Omega_{\mathrm{fS1,sg}} \end{aligned} \tag{2.10}$$

where $\omega_{\mathrm{R2,c}}$ is the calculated circular frequency of mode 14, ND 10.

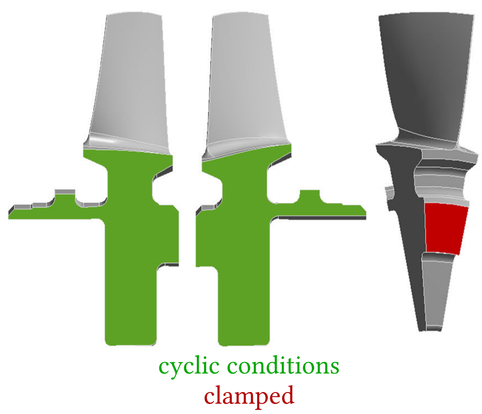

Figure 2.7: Rotor 2 clamped and cyclic BCs

The calculated natural frequencies with and without cyclic conditions were close. Moreover, the modal stress to displacement levels ratios were found to be the same for both analyses. This shows that the assumption of a non-cyclic sector is valid specifically for mode 14, ND 10, for rotor 2.

2.3 CFD Analyses

CFD analyses for predicting the transient static pressure on the blade were performed. Therefore, the goal was to perform a transient CFD analysis modelling the stator 1 and rotor 2 interactions accurately. To simulate resonance of mode 14 of rotor 2, this analysis was achieved at the rotational velocity where:

$$\Omega_{\mathrm{fS1}} = \omega_{\mathrm{R2}} \tag{2.11}$$

where Ω_{fS1} is the stator 1 excitation frequency and ω_{R2} the natural frequency of mode 14 obtained in the modal analysis of the rotor 2 sector without cyclic conditions. Based on equation (2.3) this rotational velocity is:

$$\Omega_{\mathrm{R2}} = \frac{\omega_{\mathrm{R2}}}{40} \tag{2.12}$$

For doing such a transient analysis, the BCs (entrance of stator 1 and exit of rotor 2) must be in line with the flow conditions at a rotational velocity of Ω_{R2}. However, the only known conditions were the engine inlet temperature and pressure and the corrected mass flow ($\dot{m}_{\mathrm{corr}}$) to the atmospheric pressure (p_{atm}) and temperature (T_{atm}). Therefore, the full axial compressor was modelled.

2.3.1 Inlet and Full Axial Compressor Steady Analysis

For this analysis, one passage of every component of the axial compressor and one passage of the inlet were meshed. Therefore, a total of 9 passages were included in the model which is shown in figure 2.8. in this figure, the black arrows at the entrance of the inlet passage and at the exit of the stator 4 passage are the BCs applied on theses boundaries. On the other hand, the purple arrows on the passages are the cyclic conditions.

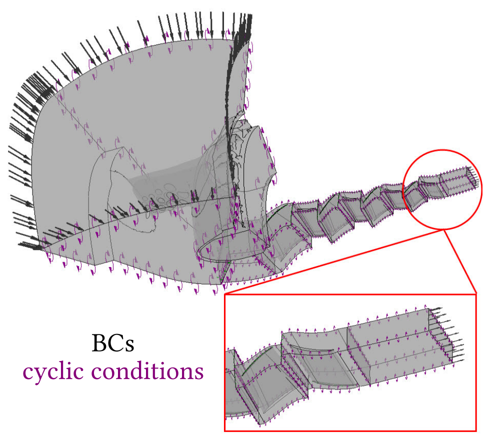

Figure 2.8: PT6 turboshaft inlet and full axial compressor CFD model

As stated above, the engine inlet temperature and pressure and the corrected mass flow to the atmospheric pressure and temperature were known. The inlet temperature and pressure are atmospheric pressure and temperature at sea level respectively. Therefore, the BC at the inlet was:

$$p_0 = p_{\mathrm{atm}}, \quad \forall x, y, z \in \partial\Omega_{\mathrm{in}} \tag{2.13}$$

where p_0 is the total pressure and $\partial\Omega_{\text{in}}$ the inlet boundary.

The BC imposed at the exit of stator 4 reads:

$$\dot{m} = \dot{m}_{\text{corr}} \sqrt{\frac{T_{\text{atm}}}{\overline{T}_{04}}} \frac{\overline{p}_{04}}{p_{\text{atm}}} \tag{2.14}$$

where $\dot{m}$ is the mass flow rate, $\dot{m}_{\text{corr}}$ the corrected mass flow to the inlet pressure and temperature, and $\overline{p}_{04}$ and $\overline{T}_{04}$ the average total pressure and temperature at the stator 4 exit respectively which are:

$$\overline{p}_{04} = \frac{1}{A} \int_{\partial\Omega_{\text{out}}} p_{04} dA \tag{2.15}$$

$$\overline{T}_{04} = \frac{1}{A} \int_{\partial\Omega_{\text{out}}} T_{04} dA \tag{2.16}$$

where p_{04} and T_{04} are the total pressure and total temperature at the stator 4 exit respectively. This set of BCs converged the analysis to flow variable quantities corresponding to the operating conditions at a rotational velocity of Ω_{R2}.

Therefore, the inlet and full axial compressor CFD model that was analyzed can be summarized as follows:

- Mesh of the inlet passage composed of tetrahedron elements and mesh of the axial component passages composed of hexahedron elements
- 4,205,120 nodes
- 6,075,734 elements
- 12,615,360 DOF

The mesh of the rotor 2 passage at mid span is shown in figure 2.9. The RANS equations, (1.9) to (1.12), were then solved using the mixing plane concept with the area averaging method introduced in section 1.2.1. The mixing plane concept had to be used since all the passages have a different pitch.

The maximum number of iterations was set to 300. After 300 iterations, convergence was satisfactory. Results such as static and total temperature and pressure, density, and velocity were verified to make sure that their values were reasonable and that the mesh size was appropriate for the flow behaviour. The mass flow rate and the stator 4 exit to the inlet pressure ratio were also verified to make sure that they were close enough to their design values for a rotational velocity of Ω_{R2}.

2.3.2 Two-Stage Axial Compressor Steady Analysis

The inlet and stages 3 and 4 were removed from the domain. Therefore, only the first two stages of the compressor (rotor 1 to stator 2) were kept. This new CFD domain is shown in figure 2.10. Notice that a small block was added downstream of stator 2 for robustness purposes. This steady analysis was also performed using the mixing plane concept with area averaging method.

The BC imposed at rotor 1 inlet is the average total pressure obtained in the inlet and full axial compressor steady analysis on this same boundary. Similarly, the same is imposed for the BC of the exit of the block downstream of stator 2, but for the static pressure instead of the total pressure.

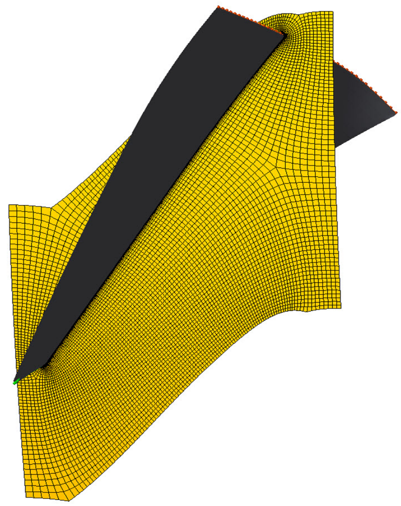

Figure 2.9: Rotor 2 passage mesh at mid span

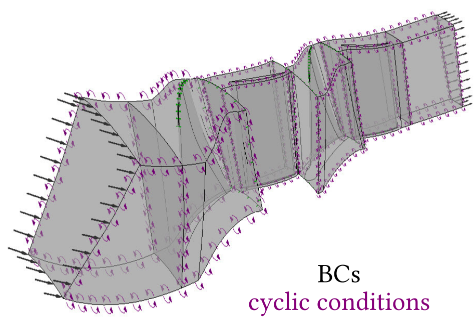

Figure 2.10: PT6 turboshaft stages 1 and 2 CFD model

The mesh of these four passages is the same as in the inlet and full axial compressor steady analysis. Therefore, the two-stage axial compressor CFD model that was analyzed can be summarized as follows:

- Mesh of the four passages and the block downstream of stator 2 composed of hexahedron elements
- 2,064,754 nodes
- 1,956,386 elements
- 6,194,262 DOF
- Converged solution of rotor 1 through stator 2 of the inlet and full axial compressor steady analysis used as flow initialization

Again, 300 iterations were performed and convergence was satisfactory. The flow variables quantity values were almost the same as what they were on the inlet and full axial compressor steady analysis which means that the imposed BCs were reproducing well the effects of the passages that have been removed. The obtained mass flow rate was the same for the inlet and full axial compressor steady analysis and the stator 2 exit to rotor 1 inlet pressure ratio was close to its design value for a rotational velocity of Ω_{R2}.

2.3.3 Two-Stage Axial Compressor Transient Analysis

The same domain and same mesh as the ones of the previous steady analysis were used. Since the flow unsteadiness occurring in the stator 1 passage must be transmitted to the rotor 2 passage, the transient analysis was done using the TBR method presented in section 1.2.1. Since the TBR method can only be used at one passage interface, the mixing plane concept with the area averaging method was used at the rotor 1 to stator 1 and rotor 2 to stator 2 interfaces.

So, the full RANS equations introduced in section 1.2.1 were solved. Rotor 1 and 2 passages were imposed a rotational velocity of Ω_{R2} and the time step size (Δt) was given as:

$$\Delta t = \frac{P_{\mathrm{S1}}}{25\Omega_{\mathrm{R2}}} \tag{2.17}$$

This time step was imposed to split the stator 1 excitation period into 25 time steps. The total time of the analysis was set to:

$$t_{\mathrm{tot}} = 2 \times 40 \times 25\Delta t \tag{2.18}$$

Therefore, the rotors did two complete rotations (720°) in 2000 time steps. At every time step, a maximum of ten iterations were allowed for residual convergence. The converged solution from the previous steady analysis was used as flow initialization for this transient analysis.

Once the analysis was completed, the static pressure history was extracted everywhere on the blade surface ($\partial\Omega_{\mathrm{fsi,R2}}$) and FFT was performed for extracting the real and imaginary static pressures at the frequency of ω_{R2}.

2.4 Harmonic Response One-Way Aeroelasticity Analysis

The total damping of the rotor 2 blade was extracted from strain gauge reading when the maximum vibratory stress ($\sigma_{\mathrm{R2,sg}}$) was recorded. More specifically, the 40ENg plot, which is shown in figure 2.2, was used for extracting the damping which was imposed to the FE model for this analysis.

For extracting the damping from an EO plot, two popular methods are the half-power bandwidth and Single Degree Of Freedom (SDOF) curve fitting methods. The curve fitting method was used in this work [3]. With this method, the damping is obtained by using the least squares method for making the best curve fit possible on the SDOF forced response steady state solution with undetermined coefficient equation which reads:

$$H(\Omega_{\mathrm{f}}) = \frac{X\omega_{\mathrm{n}}}{f_0} = \frac{1}{\sqrt{(1-r^2)^2 + (2\zeta r)^2}} \tag{2.19}$$

with:

$$r = \frac{\Omega_{\mathrm{f}}}{\omega_{\mathrm{n}}} \tag{2.20}$$

where X is the amplitude of the parameter, ω_{n} the natural frequency of the mode, f_0 the force amplitude, and Ω_{f} the imposed or forced frequency. The parameter can be any parameter for which its amplitude depends on Ω_f and ω_n such as displacement, velocity, acceleration, strain, stress, etc.

When the least squares method is applied on the SDOF steady state solution equation, the least squares function reads:

$$\prod(\zeta, \omega_\mathrm{n}, f_0) = \sum_{i}^{n_\mathrm{d}} (Y_i - X_i)^2 \tag{2.21}$$

where:

$$X_i = \frac{f_0}{\sqrt{\left(1 - (\frac{\omega_i}{\omega_\mathrm{n}})^2\right)^2 + \left(2\zeta\frac{\omega_i}{\omega_\mathrm{n}}\right)^2}} \tag{2.22}$$

and where n_d is the total number of data point considered for the curve fitting, Y_i the ith data point amplitude value, and X_i the curve fit point at the ith data point. The best possible curve fit can then be obtained by finding the appropriate f_0 and ζ values. The ζ value used for producing the best curve fit corresponds to the damping factor for the SDOF linear forced response.

The curve fitting performed on the 40ENg plot in figure 2.2 is shown in figure 2.11. The half-power line along with Ω_1 and Ω_2 are also displayed on the graph. The damping factor obtained using the SDOF curve fitting method on the 40ENg plot will be denoted as $\zeta_\mathrm{R2,sg}$.

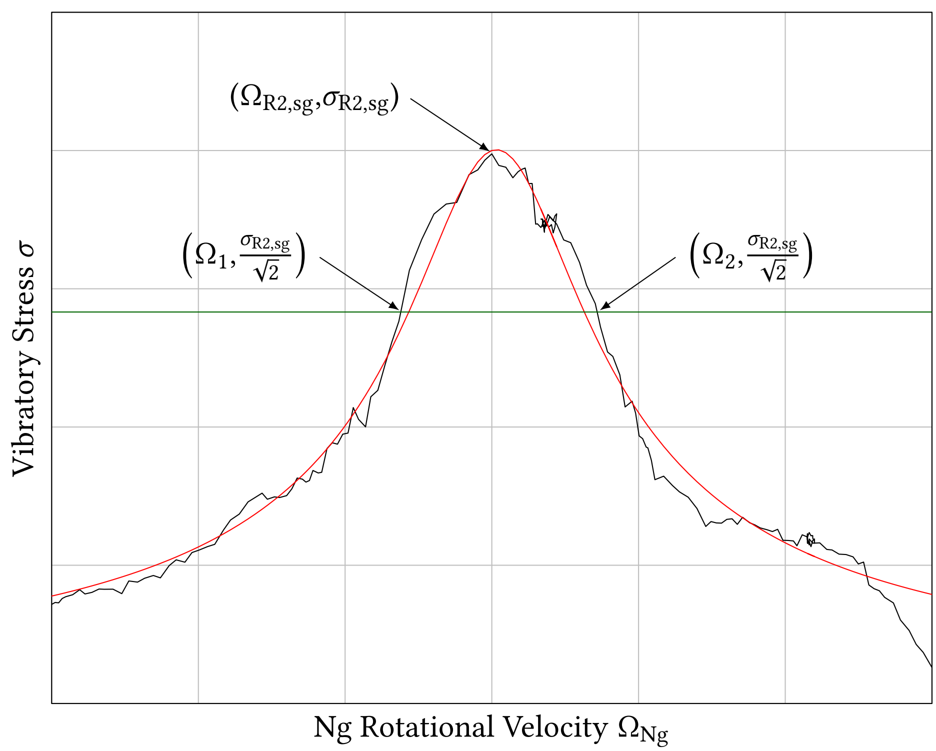

Figure 2.11: SDOF curve fit: 40ENg data (—), curve fit (—), and half-power line (—)

The harmonic response was performed using the mode superposition method which is detailed in section 1.2.2 using the results of the modal analysis detailed in section 2.2 as the modal environment. The imposed damping was set to $\zeta_{\mathrm{R2,sg}}$ and the excitation frequency was set to ω_{R2} which is the frequency for which the real and imaginary static pressures were extracted. Since the excitation frequency is set to be equal to the natural frequency of mode 14, all the energy will go into that mode which should be a good steady state representation of the instant where the $\sigma_{\mathrm{R2,sg}}$ vibratory stress was obtained in the test.

For assessing if the harmonic response one-way aeroelasticity method was giving a representative prediction of reality, the calculated σ_{11} stress at the critical location shown in figure 2.6 was compared to the experimental vibratory stress scaled at critical location ($\sigma_{\mathrm{R2,cl}}$) which can be calculated using equation (2.9). The calculated σ_{11} stress at the critical location is denoted as σ_{R2}. After comparison, it has been found that σ_{R2} was 1.34% higher than $\sigma_{\mathrm{R2,cl}}$:

$$\sigma_{\mathrm{R2}} = 1.0134\sigma_{\mathrm{R2,cl}} \tag{2.23}$$

This method is therefore extremely accurate for this test case. It is also very convenient for vibratory stress levels calculation of a mode resonating in synchronous response since it is the least expensive method in terms of computational power and time.

2.5 Transient One-Way Aeroelasticity Analysis

Since it has been found in section 2.4 that the harmonic response one-way aeroelasticity method gives excellent results in terms of vibratory stress prediction for a synchronous response, it is fair to claim that the transient one-way aeroelasticity method should not provide any added value to the results. Therefore, this method should not be preferred to the harmonic response one-way aeroelasticity method which is much less expensive in terms of computational power and time. The transient one-way aeroelasticity analysis is, however, useful to perform for validating the two-way aeroelasticity analysis setup.

A two-way aeroelasticity analysis would actually bring an added value to the prediction since the total damping ($\zeta_{\mathrm{R2,sg}}$) does not need to be provided. The only damping that would need to be provided is the material damping which is well known, but the aerodynamic damping effects are part of the two-way aeroelasticity computation as explained in section 1.2.5.

Therefore, the transient one-way aeroelasticity of rotor 2 was performed as a preparatory work for the two-way aeroelasticity analysis. The same FE model as the one used for the modal analysis was used. The same time step size as the one set in the transient CFD analysis was imposed. As stated in section 1.2.2, the amplitude decaying factor (γ) was set to zero since high frequency phenomena should not be attenuated. All the static pressure time history calculated in the transient CFD analysis described in section 2.3 was mapped on the blade surface ($\partial\Omega_{\mathrm{fsi,R2}}$) before undertaking the analysis and the imposed damping was $\zeta_{\mathrm{R2,sg}}$.

The Initial Condition (IC)s of the analysis were the following:

$$\begin{aligned} \{u(t=0)\} &= \{0\} \\ \{\dot{u}(t=0)\} &= \{0\} \end{aligned} \tag{2.24}$$

For applying the constant loads (centrifugal and thermal) at every time step without shocking the system, time integration was turned off for the two first time steps. Consequently, the system of equations reduced to:

$$\{F_{\mathrm{el}}(\{u\})\} = [K(\{u\})]\{u\} = \{F\} \tag{2.25}$$

So, only the Newton-Raphson algorithm is required for solving this system of equations. For the first time step, the aerodynamic pressure mapping was not considered. The obtained nodal displacements ($\{u\}$) were the displacements corresponding to a time $t = \Delta t$. Therefore, the nodal velocity vector at this time step was:

$$\{\dot{u}(t = \Delta t)\} = \frac{\{u(t = \Delta t)\} - \{u(t = 0)\}}{\Delta t} \tag{2.26}$$

which combined with equation (2.26) yields:

$$\{\dot{u}(t = \Delta t)\} = \frac{\{u(t = \Delta t)\}}{\Delta t} \tag{2.27}$$

For the second time step, the aerodynamic pressure mapping for the first transient CFD time step was imposed with the thermal and centrifugal loads. The obtained results were therefore for time $t = 2\Delta t$. The velocity vector was:

$$\{\dot{u}(t = 2\Delta t)\} = \frac{\{u(t = 2\Delta t)\} - \{u(t = \Delta t)\}}{\Delta t} \approx 0 \tag{2.28}$$

The only difference between the displacement vectors at $t = \Delta t$ and $t = 2\Delta t$ was the impact of the aerodynamic static pressure mapping which was negligible since Δt was small. For the remaining time steps, time integration was turned on and the complete transient system of equations was solved.

To assess if mode 14 was in resonance as expected, the σ_{11} and σ_{33} stress levels at mode 14 critical location shown in figure 2.6 were plot as a function of time. This plot is shown in figure 2.12. It could be observed by looking at mode 14 critical location stress vs. time graph that mode 14 is in resonance since the σ_{11} and σ_{33} stress levels were getting higher and higher at every cycle. On the other hand, it could also be observed that the stress levels had not reach their maximum values when the analysis was completed since they were still on an increasing trend. Note as well that the stress levels do not start from the zero line and that the σ_{33} stress was higher than the σ_{11} stress. This is because these stress levels were the total ones (steady plus vibratory stress levels). Since the steady loads induce a σ_{33} stress at the critical location, the σ_{33} stress begins from a non-zero value. These results indicate that the analysis was setup properly. Accordingly, it was worth undertaking a two-way aeroelasticity analysis.

2.6 Two-Way Aeroelasticity Analysis

As explained in section 1.2.5, the transient CFD and FE analyses are solved simultaneously in a two-way aeroelasticity analysis. Moreover, mesh morphing (or mesh deformation) occurs in the fluid domain. Since the fluid domain undergoes mesh morphing, the transient analysis cannot be done using the TBR method. Therefore, the pitch scaling method described in section 1.2.1 was used since the flow unsteadiness of stator 1 needed to be modelled and transmitted to rotor 2. Consequently, stator 1 and rotor 2 passages were added to the fluid domain used in the previous transient CFD analysis to make $P_R = P_S$. The fluid domain used for the transient CFD analysis is shown in figure 2.13.

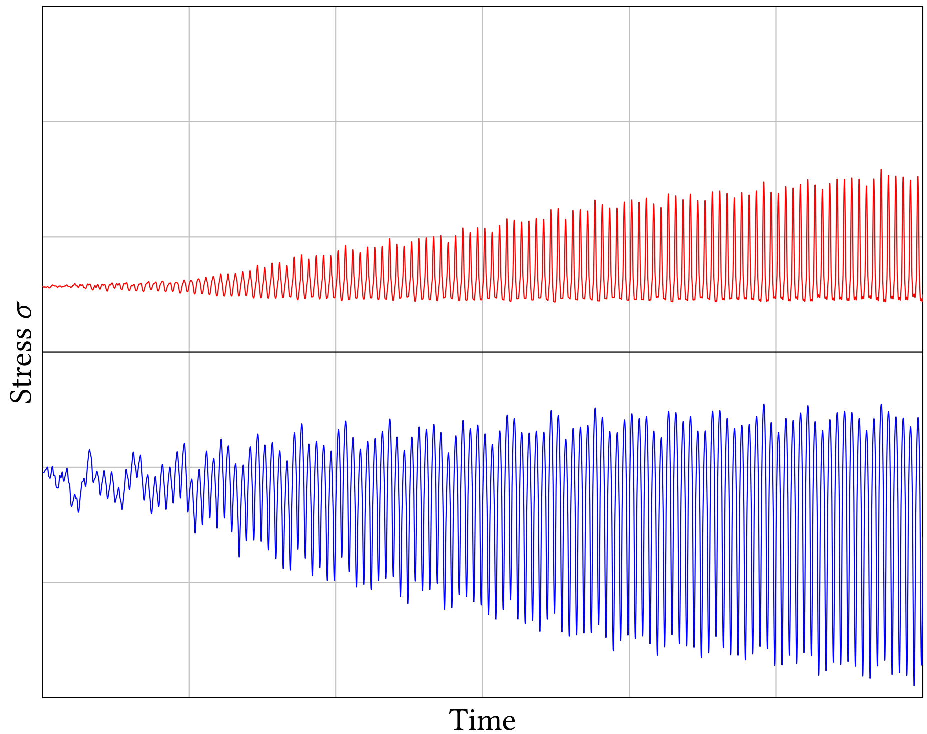

Figure 2.12: Stress vs. time for 2,000 time steps: σ_{11} (——) and σ_{33} (——)

With a rotor 2 composed of 25 blades and a stator 1 composed of 40 vanes, 8 stator 1 passages and five rotor 2 passages were required since:

$$P_R = P_S = 72^\circ \tag{2.29}$$

Therefore, the analyzed CFD model can be summarized as follows:

- Mesh of all the passages and the block at the stator 2 exit composed of hexahedron elements
- 7,463,582 nodes
- 7,056,277 elements

First, a steady CFD analysis was performed on this domain. The converged flow obtained in the passages of the stage 1 and 2 CFD steady analysis detailed in section 2.3.2 was used as flow initialization for this steady analysis. The boundary conditions were also the same as the steady analysis in section 2.3.2. This steady analysis was done for the same reasons as the steady analysis in section 2.3.2.

The converged flow obtained with this steady analysis was used as flow initialization for the CFD transient analysis portion of the two-way aeroelasticity analysis. The coordinates of solid domain blade corresponded to the coordinates of the center rotor 2 blade in the fluid domain. This blade surface was, therefore, the fluid-structure interface.

The two-way aeroelasticity analysis was launched using the same time step size as in the one-way aeroelasticity analyses. On the FE side, time integration was turned off for the two first time steps for the same reasons explained in section 2.5. However, mesh folding occurred in the fluid domain and the analysis failed.

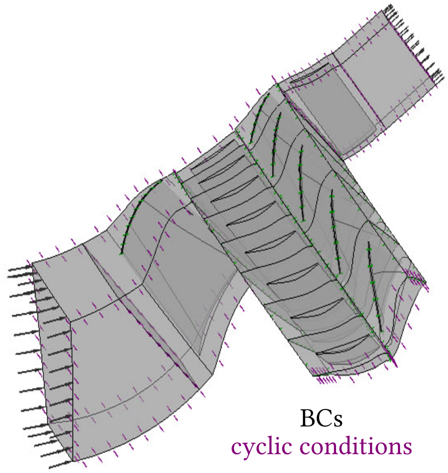

Figure 2.13: PT6 turboshaft stages 1 and 2 CFD model for two-way aeroelasticity

It was attempted to correct by changing some mesh rigidity criteria in the fluid domain, but the attempts were unsuccessful. It was therefore decided to stop the two-way aeroelasticity analysis. If this analysis is re-attempted in the future, the suggested approach is to impose different fluid domain mesh rigidity criteria especially for the nodes and elements located near the fluid-structure interface since this is where folding occurred.

Chapter 3

Aeroelasticity Analyses on PT6 Turbopropeller Compressor Stator 1 Vane

3.1 Strain Gauge Test Results Review

The potential sources of excitation of the stator 1 should be obtained. The concepts explained at the beginning of section 2.1 apply for this stator. However, components that can induce considerable excitation are the rotor and impeller blades. Since every rotor is mounted on the same shaft (Ng) in a PT6 engine, any aerodynamic periodic excitation is:

$$\Omega_{\mathrm{fR}} = N_{\mathrm{b}} \omega_{\mathrm{Ng}} \tag{3.1}$$

where N_{b} is the number of blades on the rotor or impeller. Accordingly, the EO is defined as:

$$E_{\mathrm{O}} = N_{\mathrm{b}} = \frac{\Omega_{\mathrm{fR}}}{\omega_{\mathrm{Ng}}} \tag{3.2}$$

For the case of this PT6 turbopropeller, when stator 1 was experiencing its highest vibratory stress, the EO was equal to 16. Consequently, rotor 1 was identified as the source of excitation. The engine run where the highest vibratory stress occurred was performed under two different inlet temperature conditions. For the first condition, the inlet temperature was at a temperature T_{c1} and for the second condition, it was at a temperature T_{c2} where T_{c2} is 50% higher than T_{c1}:

$$T_{\mathrm{c2}} = 1.5 T_{\mathrm{c1}} \tag{3.3}$$

The waterfall plot in figure 3.1 shows the highest vibratory stress recorded which was when the inlet temperature was T_{c2}.

This vibratory stress is called $\sigma_{\mathrm{sg,c2}}$. To better observe the differences between the vibratory stress levels for the two conditions, the resonance is shown on the zoomed 16ENg plot in figure 3.2.

From the 16ENg graph, it was observed that:

$$\sigma_{\mathrm{sg,c2}} = 1.359 \sigma_{\mathrm{sg,c1}} \tag{3.4}$$

Also, the resonance natural frequency is slightly higher at the first condition. It was found that:

$$\Omega_{\mathrm{fR1,sg,c1}} = 1.004 \Omega_{\mathrm{fR1,sg,c2}} \tag{3.5}$$

This difference in natural frequency is negligible. It probably occurs because the temperature and average pressure on the vane are slightly different due to the difference in inlet temperature. The obtained natural frequencies in the analyses is compared with the excitation frequency of condition 1 which, form now on, will be called $\Omega_{\mathrm{fR1,sg}}$. Similarly, the rotational velocity at which the excitation frequency occurred with the first condition will be called $\Omega_{\mathrm{S1,sg}}$.

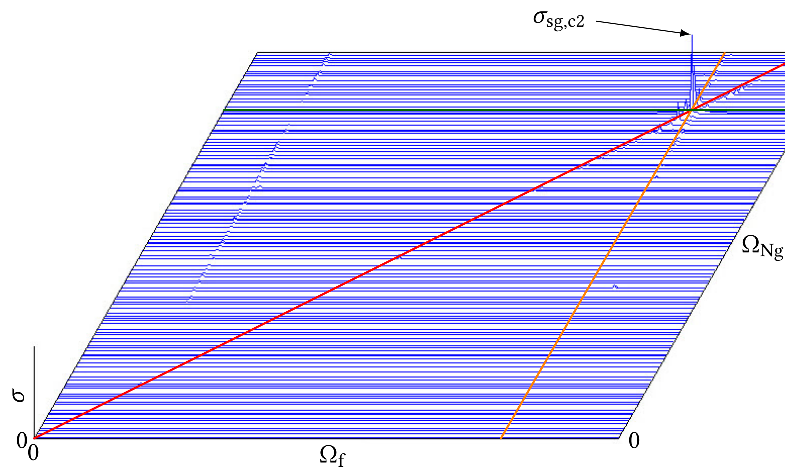

Figure 3.1: Waterfall plot: strain gauge data (——), 16ENg (——), $\Omega_{fR1,sg,c2}$ (——), and $\Omega_{sg,c2}$ (——)

3.2 Modal Analyses

As explained in section 3.1, stator 1 was excited by rotor 1 which is composed of 16 blades. As for the rotor 2 test case, stator 1 ND in resonance for excitation coming from rotor 1 has to be calculated. The same rules as equations (2.4) and (2.5) apply on stator 1. The possible NDs for a stator depending on the number of vanes (N_v) is:

$$0 \leq N_D \leq \frac{N_v}{2} \tag{3.6}$$

and if the number of vanes is odd, the possible NDs are any integer satisfying:

$$0 \leq N_D \leq \frac{N_v - 1}{2} \tag{3.7}$$

Again, the ND in resonance can be found by aliasing using the following equation:

$$N_D = -E_O + n_i N_v \tag{3.8}$$

Since the stator 1 is subjected to a 16ENg excitation coming from the 16 blade rotor 1, the ND in resonance is 16.

With this test case, considering only a one vane sector in the FE analysis was not a valid assumption. As opposed to the rotor 2 test case, the stator 1 vane is attached to a very thin shroud which is very flexible and undergoes a considerable amount of modal displacements even for high NDs. The FE analyses were performed on two different models: a three vane sector and a full 360° model with the 40 vanes. Obviously, the 40 vane model is the best possible representation of reality in terms of solid mechanics. However, it is a very large model in terms of mesh size and DOF and is therefore very expansive in terms of time and computational effort. The three vane model was analyzed as well to see if this reduced model was a reasonable assumption. The reason why three vanes were chosen is that when ND 16 is in resonance on a 40 vane stator, modes periods repeat themselves at every 2.5 vanes:

$$2.5 = \frac{40}{16} \tag{3.9}$$

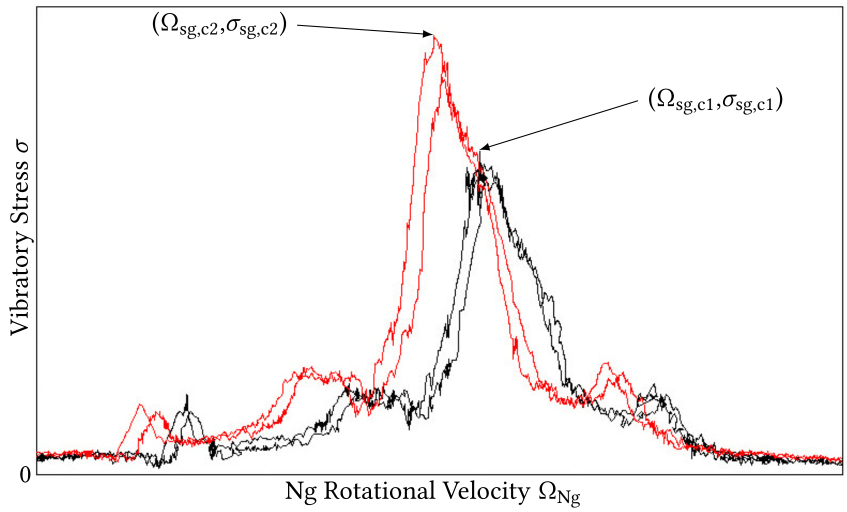

Figure 3.2: 16ENg plot: 16ENg strain gauge data for condition 1 (—) and condition 2 (—)

The two models were meshed to be analyzed. The mesh at the vane level is shown in figure 3.3.

Figure 3.3: Vane mesh of stator 1

The clamped BCs applied on the three vane model are shown in figure 3.4. The two bottom images in figure 3.4 show the three vane model with all DOF clamped BCs on the cyclic faces. These BCs are therefore not present on the 40 vane model which only has the BCs on the flange shown on the top images in figure 3.4 along the circumference. The FE models that were analyzed can be summarized as follows:

- Mesh composed of quadratic tetrahedron elements on the 2 models
- On the three vane model:
  - 1,213,229 nodes
  - 803,360 elements
  - 3,639,687 DOF on the complete model
  - 5,167 nodes affected by the clamped all DOF BCs
  - 3,624,186 DOF on the reduced model due to BCs

- On the 40 vane model:
  - 9,987,389 nodes
  - 6,635,971 elements
  - 29,962,167 DOF on the complete model
  - 1,566 nodes affected by the clamped all DOF BCs
  - 29,957,469 DOF on the reduced model due to BCs

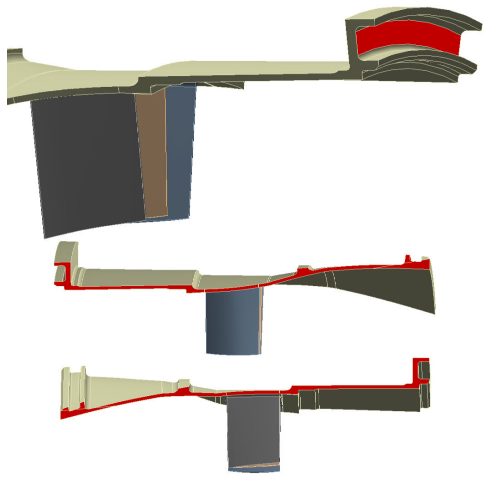

Figure 3.4: Stator 1 clamped all DOF BC

As explained in section 1.2.2, the modal analysis of stator 1 was performed in a prestress environment like the rotor 2 test case. The difference with rotor 2 test case is that the thermal load is the only load considered in the prestress environment. Again, the gaspath load or the average pressure load has some impact on the steady state of the vane, but negligible impact from a prestress environment point of view. The temperature distribution on stator 1 at a rotational velocity of $\Omega_{S1,sg}$ was imposed to the FE models.

The modal analyses were performed on the two models by solving the system of equations (1.50). The natural frequencies, modal deflection, strain, and stress levels were calculated. By looking at the obtained natural frequency levels on the two models, the fourth mode, which is the second bending mode of the vane, was identified as the closest frequency to $\Omega_{fR1,sg}$. The considered second bending mode shape on the 40 vane model was the ND 16 one. On the other hand, on the three vane model, the considered second bending mode shape was the one shown in figure 3.5 which was the mode where the middle vane had the maximum modal displacements. Since the middle vane was the farthest vane from the all DOF clamped BCs on the cyclic faces, it was the one attached to the most flexible part of the shroud.

In the three vane model, the natural frequency of mode 4 shown in figure 3.5 was 3.46% higher than the natural frequency during the test:

$$\omega_{R2,3v} = 1.0346\Omega_{fR1,sg} \tag{3.10}$$

One the other hand, the natural frequency of mode 4, ND 16, for the 40 vane model was 3.55%

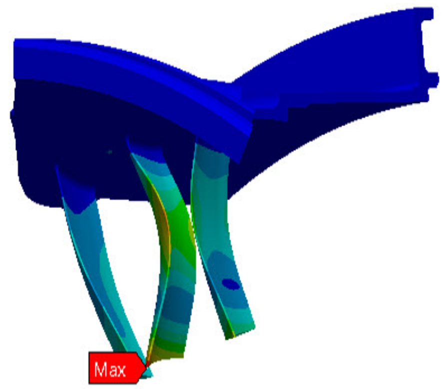

Figure 3.5: Rotor 2 mode shape of mode 4

higher than the natural frequency during the test:

$$\omega_{\mathrm{R2,40v}} = 1.0355\Omega_{\mathrm{fR1,sg}} \tag{3.11}$$

The calculated natural frequencies ware therefore close to the one in the test and were also close to each other. This is an indication that the three vane model may be reasonable.

From the results of both models, the σ_{11} stress distribution was plotted and was found to be the same. The maximum modal stress to displacement levels ratio was also the same on both models which is another indication that the three vane model may be a reasonable assumption. The obtained σ_{11} stress distribution on the pressure side is shown in figure 3.6. This figure shows the secondary critical location which was at the trailing edge mid-span. The primary critical location was at the fillet radius leading edge. This region had zero σ_{11} stress when the secondary critical location experiences its maximum σ_{11} value. Actually, the secondary critical location experienced its maximum σ_{11} stress 180° later than the primary critical location in terms of phase.

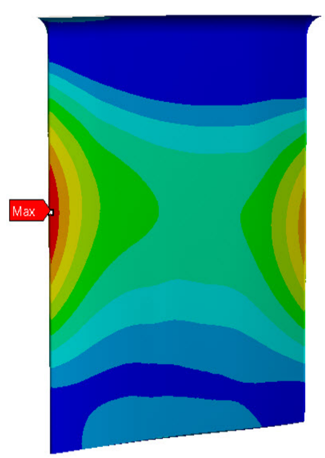

Figure 3.6: Stator 1 σ_{11} stress distribution on the pressure side for mode 4

Analytical vs. experimental stress comparisons were performed with the secondary critical location because the stress at the primary critical location was highly concentrated which made the stress value highly dependent on mesh density. Moreover, using the secondary critical location for doing the analytical vs. experimental stress comparison, the scaling factor between the stress read by the gauge and the stress at secondary critical location was unity. So, the calculated stress values were compared to the stress values read by the strain gauge directly.

3.3 Harnonic Response One-Way Aeroelasticity Analyses

The CFD analyses required for doing one-way aeroelasticity are of exactly the same type as the ones performed for the rotor 2 test case which are detailed in section 2.3. Therefore, they are not detailed for this test case. Two steady and unsteady sets of CFD analyses have been performed: one with an inlet temperature of T_{c1} for modelling condition 1 and one with an inlet temperature of T_{c2} for modelling condition 2. This section focuses only on the harmonic response analyses using the real and imaginary static pressures extracted from the unsteady CFD analysis.

The first step of the harmonic response analysis was to extract the damping from the test data. This extraction was performed through the SDOF curve fitting method described in section 2.4. The SDOF curve fitting was performed on the resonances where $\sigma_{sg,c1}$ and $\sigma_{sg,c2}$, which are shown in figure 3.2, were recorded. The obtained damping factors were extremely close to each other. The difference was judged negligible. The damping factor obtained from the curve fitting performed on the $\sigma_{sg,c2}$ resonance was chosen as the damping input for the harmonic analyses and is denoted as $\zeta_{S1,sg}$. The SDOF curve fitting and half-power lines are shown in figure 3.7.

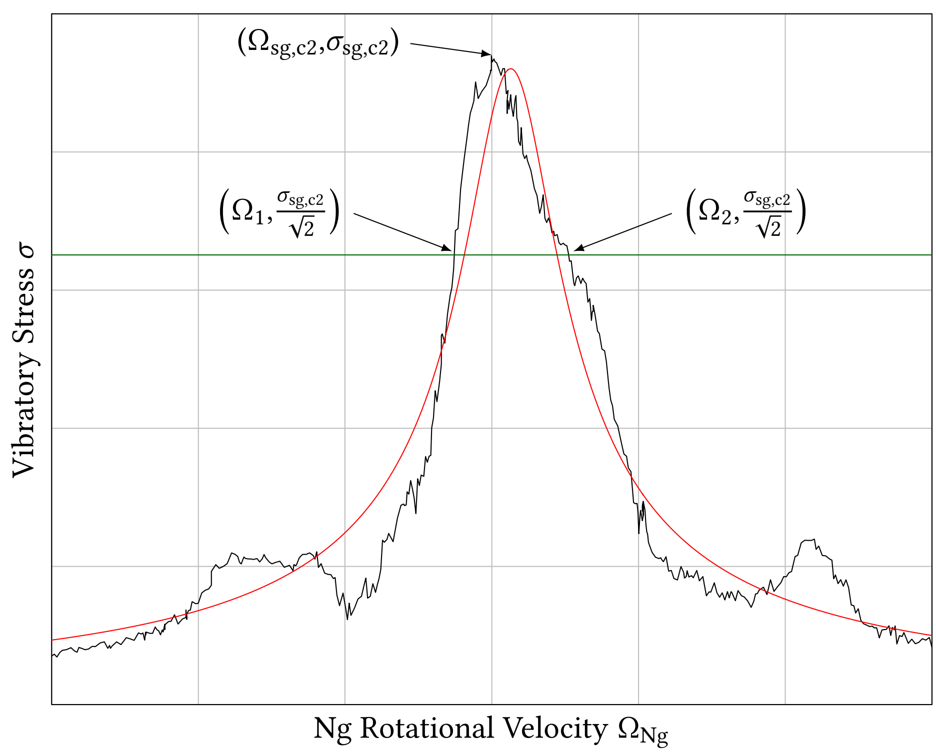

Figure 3.7: SDOF curve fit: 16ENg data (—), curve fit (—), and half-power line (—)

The second step in the harmonic analysis was to map the real and imaginary pressures extracted from the unsteady CFD analyses which were run at a rotational velocity of $\Omega_{S1,sg}$. Therefore, these pressures were extracted for the frequency of $\Omega_{fR1,sg}$. Since the unsteady CFD analyses were performed using the TBR method for the two conditions, only one stator 1 vane was modelled. However, the two FE models are composed of more than one vane. So, the real and imaginary pressures were duplicated and mapped on the other vanes present in the FE models. The phase difference of the aerodynamic force between each vane was considered in the duplication of these pressures. For this particular case, the phase difference ($\Delta\phi$) is:

$$\Delta\phi = 2\pi \frac{E_{\mathrm{O}}}{N_{\mathrm{V}}} = 2\pi \frac{16}{40} = 0.8\pi \tag{3.12}$$

The harmonic response analyses were run and a damping factor of ζ_{S1} was imposed. As mentioned previously, the real and imaginary pressures were extracted at the frequency of $\Omega_{fR1,sg}$ because the rotational velocity that was used in the unsteady CFD analyses was the one when resonance occurred in test. To get the maximum possible vibratory stress in the harmonic response analyses, the excitation frequency imposed in the 3 vane and 40 vane models analyses were $\Omega_{R2,3v}$ and $\Omega_{R2,40v}$ respectively. In the rotor 2 test case, this modification was not necessary since the unsteady CFD analysis was run at the rotational velocity for which the excitation frequency was equal to the natural frequency of mode 14.

With the 3 vane model, the calculated vibratory stress at the secondary critical location shown in figure 3.6 was 27.1% less than in test for condition 1 and 39.5% less than in test for condition 2:

$$\sigma_{3v,c1} = 72.9\sigma_{sg,c1} \tag{3.13}$$

$$\sigma_{3v,c2} = 60.5\sigma_{sg,c2} \tag{3.14}$$

On the other hand, with the 40 vane model, the calculated vibratory stress at the secondary critical location shown in figure 3.6 was 29.2% less than in test for condition 1 and 41.4% less than in test for condition 2:

$$\sigma_{40v,c1} = 70.8\sigma_{sg,c1} \tag{3.15}$$

$$\sigma_{40v,c2} = 58.6\sigma_{sg,c2} \tag{3.16}$$

It could be observed that the 3 and 40 vane models results are close; so, the 3 vane model approximation was reasonable. However, it was also observed that the results do not match the test results as well as in the rotor 2 test case. Moreover, the error is greater with condition 2.

By looking at the unsteady CFD analysis results, flow separation has been observed on the inside and outside diameters of the vane for the two conditions. Flow separation for the two conditions is shown on the Mach number plots at the outside diameter in figure 3.8. These plots were generated from the unsteady CFD analyses at a certain time step. In figure 3.8a, it was observed that a Laminar Separation Bubble (LSB) is present near the leading edge and that the flow separates a little after mid-chord. On the other hand, it was observed in figure 3.8b that the flow separates from leading edge to trailing edge meaning that the vane is fully stalled for the outside and inside diameters. Therefore, the separated flow region is much bigger for condition 2.

There is a clear correlation between the analytical vs. experimental stress differences and the size of the separated flow region. This indicates that the separated flow may be the source

(a) Condition 1: flow separation

(b) Condition 2: stalled

Figure 3.8: Mach number plots at outside diameter

of error. This makes sense because as explained in section 1.2.1 the RANS equations do not model the resolution of the fluctuations in turbulent regions. Since the separated flow regions are turbulent regions, the RANS equations may be missing some important fluctuations that could have a considerable impact on the static pressure on the suction side of the vane.

The best approach to verify this hypothesis would be to run the unsteady CFD analyses using Large Eddy Simulation (LES). With LES, the resolution of the fluctuations are modelled. Therefore, if the hypothesis is correct, more accurate stress predictions are the expected outcomes if the harmonic response one-way analysis is relaunched using LES in the unsteady CFD analyses.

Chapter 4

Conclusion

4.1 Accomplishments

Two one-way aeroelasticity analysis procedures have been established: harmonic response and transient. The procedure is to perform a set of steady CFD analyses starting from the full axial compressor and reducing the model to the components of interest. These steady CFD analyses ensure that small and convenient CFD models can be used with accurate BCs. Then, an unsteady CFD analysis is performed to model the time varying static pressure on the investigated blade or vane. Finally, the harmonic response or transient FE analysis is performed using damping extracted from strain gauge data to calculate the vibratory stress levels.

The harmonic response analysis is the fastest and easiest one-way aeroelasticity method since it is a time independent approach. It was performed with the mode superposition method in this project. P&WC is going to use this methodology when performing vibratory stress predictions using one-way aeroelasticity. The downside of this type of analysis is that aerodynamic damping input is required since it cannot be captured in the analysis. It may be difficult to do vibratory stress predictions for blades and vanes of a new engine for which no strain gauge data is available.

The harmonic response one-way aeroelasticity analysis methodology has been validated using two test cases: the PT6 turboshaft rotor 2 blade and the PT6 turbopropeller stator 1 vane. The vibratory stress prediction on the rotor 2 blade was 1.34% higher than the vibratory stress in test. Therefore, the analysis prediction is representative of reality for this case.

On the other hand, the vibratory stress predictions were not accurate on the stator 1 test case. Two FE models were considered: a 3 vane sector and the full stator with its 40 vanes. The engine was tested with 2 different inlet temperatures. the second inlet temperature was 50% higher than the first one. This increased the maximum vibratory stress by 35.9%. These 2 inlet temperature conditions were modelled and the vibratory stress levels were calculated. With the full stator model, the calculated vibratory stress was 29.2% less than in test for the first inlet temperature and 41.1% less than in test with the second one. The presence of separated flow regions is a potential source of error since the RANS equations do not model the resolution of the fluctuations in turbulent flows.

The transient one-way aeroelasticity method has been validated using the rotor 2 test case. It requires much more time and computational power for solving than the harmonic response method and does not offer extra benefits. It is therefore not worth doing this type of analysis if one-way aeroelasticity only is performed. On the other hand, if a two-way aeroelasticity needs to be performed, it is highly recommended to perform this analysis since two-way aeroelasticity can only be performed with a transient FE analysis. The transient one-way aeroelasticity analysis should be used to ensure that the FE model is properly set up and that the mode for which the vibratory stress levels are needed is in resonance.

Finally, a two-way aeroelasticity analysis was performed on the rotor 2 test case, but the analysis failed due to mesh folding in the CFD domain. All the different CFX mesh rigidity parameters were tried, but none of them prevented the mesh from folding. The methodology for performing such an analysis was established, but not validated because of this issue.

4.2 Proposed Future Work

The harmonic response one-way aeroelasticity analysis will be repeated on other geometries to verify that the accuracy of this type of analysis is systematic. This will indicate to what point this type of analysis can be trusted. The unsteady CFD analyses of the stator 1 test case may be relaunched with LES and the vibratory stress levels re-predicted to validate that the lack of accuracy was because of flow separation.

If it is systematically accurate, this methodology will be used for predicting vibratory stress levels on blade and vane redesigns. The damping will be extracted from the strain gauge test of the blade or vane primary designs and used in the analyses. Since redesigns usually have only minor changes, damping should not be affected. Therefore, a strain gauge test on the redesign may be avoided in such circumstances. This methodology will also be used for blade and vane designs of new engines for which no test exists. However, its validity will have to be verified because the damping has to be assumed since it cannot be extracted from a test. This would not avoid doing a strain gauge test since the damping value may not be accurate. However, it may help to identify potentially dangerous modes that should be tuned out, hence reducing the chance of failing the strain gauge test because of too high vibratory stress levels.

Finally, the mesh folding issue should be resolved by defining other mesh rigidity parameters and imposing them to CFX until the issue is resolved. Once this is resolved, it should be tested like the harmonic response method to see if predictions are good. This analysis could produce more accurate predictions since aerodynamic damping is calculated in the CFD analysis. It would therefore be very useful for new engine blade and vane designs. Two-way aeroelasticity could also be used for predicting flutter.

Bibliography

[1] George Batchelor. *An Introduction to Fluid Dynamics.* Cambridge University Press, 1967.

[2] Klaus-Jürgen Bathe. *Finite Element Procedures.* Pearson Education, 2006.

[3] Chris Beards. *Structural Vibration: Analysis and Damping.* John Wiley & Sons, 1996.

[4] Ted Belytschko and Jacob Fish. *A First Course in Finite Elements.* John Wiley & Sons Ltd, 2007.

[5] Robert Clark and Earl Dowell. *A Modern Course in Aeroelasticity.* Kluwer Academic Publishers, 4 edition, 2004.

[6] Iain Currie. *Fundamental Mechanics of Fluids.* CRC Press, 4 edition, 2013.

[7] ANSYS Inc. *ANSYS Mechanical APDL Theory Reference.* 2013.

[8] ANSYS Inc. *ANSYS CFX-Solver Theory Guide.* 2013.

[9] ANSYS Inc. *ANSYS Fluent Theory Guide.* 2013.